

Fracture behaviour of functionally graded bi-material interface produced by wire arc additive manufacturing

Galán Argumedo, J. L.; Riemslag, A. C.; Hermans, M. J.M.; Popovich, V. A.

DOI

[10.1016/j.msea.2025.148034](https://doi.org/10.1016/j.msea.2025.148034)

Publication date

2025

Document Version

Final published version

Published in

Materials Science and Engineering: A

Citation (APA)

Galán Argumedo, J. L., Riemslag, A. C., Hermans, M. J. M., & Popovich, V. A. (2025). Fracture behaviour of functionally graded bi-material interface produced by wire arc additive manufacturing. *Materials Science and Engineering: A*, 928, Article 148034. <https://doi.org/10.1016/j.msea.2025.148034>

Important note

To cite this publication, please use the final published version (if applicable). Please check the document version above.

Copyright

Other than for strictly personal use, it is not permitted to download, forward or distribute the text or part of it, without the consent of the author(s) and/or copyright holder(s), unless the work is under an open content license such as Creative Commons.

Takedown policy

Please contact us and provide details if you believe this document breaches copyrights. We will remove access to the work immediately and investigate your claim.



Fracture behaviour of functionally graded bi-material interface produced by wire arc additive manufacturing

J.L. Galán Argumedo^{*} , A.C. Riemslag , M.J.M. Hermans, V.A. Popovich

Department of Materials Science and Engineering, Delft University of Technology, the Netherlands

ARTICLE INFO

Keywords:

Wire arc additive manufacturing
Functionally graded material
Bi-material interface
Fracture toughness

ABSTRACT

Wire arc additive manufacturing (WAAM) offers a novel approach to fabricate functionally graded components. By changing the wire consumable between layers, chemical grading can be used to obtain specific properties across a part's volume. This is an interesting approach to design large metal components that achieve unconventional performance in demanding engineering applications, such as sulphide-resistant pressure vessels or sea ballast piping with extended lifetime. However, challenges derived from dissimilar material combinations draw the need to study the effect of compositional grading on the mechanical properties. This study focuses on the deformation and fracture toughness behaviour of WAAM-fabricated high-strength low-alloy (HSLA) and austenitic stainless (AS) steel bi-material specimens, particularly examining the diluted interface layer obtained during deposition. Tensile testing results indicate that the elastic modulus at the interface matches that of undiluted AS steel (157 ± 17 GPa) along the build direction. Fracture toughness showed a lower J_{IC} (180 kJ/m^2) when compared to the undiluted AS steel ($459 \pm 69 \text{ kJ/m}^2$) and HSLA steel ($408 \pm 25 \text{ kJ/m}^2$). Scanning electron microscopy and electron backscatter diffraction are used to establish a connection between the microstructure at the interface and the observed mechanical properties. It is concluded that deformation at the interface is in large controlled by the deformation-induced martensitic transformation of metastable austenite. These results underline the influence of chemical dilution on the deformation mechanisms and fracture behaviour of HSLA and AS steel bi-material parts, which needs to be accounted for in the design of parts composed by this bi-metal couple.

1. Introduction

Wire arc additive manufacturing (WAAM) enables the construction of large, functionally graded parts [1]. Following the principles of direct-energy deposition, a robot-assisted arc welding system can deposit material at rates unmatched by other metal additive manufacturing processes [2], with the potential to create features extending up to meter-scale lengths. A large availability of welding wire consumables can be exploited to additively-manufacture parts of all commercially available alloy families [3]. For some alloys, process parameter modulation can be used to control heating and cooling processes, causing microstructural gradients and thus a graded functional performance [4].

The material flexibility available to the WAAM process can also be exploited to produce parts consisting of dissimilar alloys, with the objective to produce highly optimized compositionally graded components with tuned functional properties. Examples in literature exist for

many material combinations. Wang et al. [5] produced a continuous gradient of pure titanium to Ti-50 at% Al alloy with tandem-WAAM, resulting in a defect-free build with tuned mechanical and oxidation behaviour. The authors highlight the connection between the phases obtained through dilution of both alloys and their effect on the functional properties measured. Rodrigues et al. [6] achieved a smooth hardness and electrical conductivity gradient between a CuAl alloy and a HSLA steel. Dilution of the alloys at the interface region led to a mixture of Cu (FCC) and Fe (BCC) phases that proved useful to bridge the differences in functional properties between both alloys. Wu et al. [7] showed that by interweaving the deposition of a HSLA steel and a Ni-3.5 wt% Ti alloys, hierarchical structuring combined with solid solution strengthening at the interface produce a component stronger than the original feedstock materials. A duplex stainless steel was graded with HSLA steel to produce a corrosion resistant section for marine risers by Chandrasekaran et al. [8]. The dilution of both alloys lead to a martensite layer that provided additional strength under tensile loading. These, and many more examples, offer valuable evidence on the

^{*} Corresponding author.

E-mail address: j.l.galanargumedo@tudelft.nl (J.L. Galán Argumedo).

<https://doi.org/10.1016/j.msea.2025.148034>

Received 8 July 2024; Received in revised form 3 February 2025; Accepted 9 February 2025

Available online 12 February 2025

0921-5093/© 2025 The Author(s). Published by Elsevier B.V. This is an open access article under the CC BY license (<http://creativecommons.org/licenses/by/4.0/>).

List of symbols and abbreviations

Lower case symbols

a	Crack length [mm]
a_p	Final crack length before final tear-out [mm]
a_0	Initial crack length after pre-fatigue [mm]
b_0	Remaining tendon ahead of a_0 [mm]
e	Engineering strain [–]
e_m	Relative error function between $CMOD_{Analyt}$ and $CMOD_{FEM}$ [–]
$e_{a/W}$	Inverse function of e_m [–]
$f\left(\frac{a}{W}\right)$	Geometry-specific function relating P and K [–]
i	Counter variable indicating a given load-unload cycle
s	Engineering stress [MPa]
u	Function-specific substitution variable [–]
v_{LL}	Load-line displacement [mm]
v_m	Crack-mouth opening displacement [mm]

Upper-case symbols

AS	Austenitic Stainless
B	Specimen thickness, before grooving [mm]
B_n	Specimen thickness, after grooving [mm]
B_e	Effective specimen thickness [mm]
BM	Bi-material
$C(a/W)_{FEM,BM}$	Relative crack depth as a function of compliance, as derived from linear-elastic FEM results [mm/mm]
$C(a/W)_{Analyt,MM}^E$	Relative crack depth as a function of CMOD compliance, as derived from linear-elastic FEM results [mm/mm]
C_{LL}	Load-line compliance [mm/N]
C_m	Crack-mouth opening displacement compliance [mm/N]
$C_{m,analyt}$	Analytical description of crack-mouth opening displacement compliance [mm/N]
$CMOD$	Crack-mouth opening displacement [mm]
$CMOD_{Analyt}$	Analytical description of crack-mouth opening displacement [mm]
$CMOD_{BM}$	Numerical description of crack-mouth opening displacement for a bi-material specimen [mm]
$CMOD_{FEM}$	Numerical description of crack-mouth opening

	displacement, as obtained by FEM [mm]
$CMOD_{MM}$	Numerical description of crack-mouth opening displacement for a mono-material specimen [mm]
E	Elastic modulus [MPa]
G_I	Elastic energy per unit area of crack extension [kJ/m ²]
G_{MM}^E	Elastic energy per unit area of crack extension for a mono-material specimen of elastic modulus E [kJ/m ²]
HSLA	High Strength Low Alloy
$J_{I,el}, J_{el}$	Elastic component of J-integral [kJ/m ²]
J_{Ic}	Classified, size-insensitive plane strain fracture toughness
$J_{el,BM}$	Numerical description of elastic component of J-integral for a bi-material specimen [kJ/m ²]
J_{pl}	Plastic component of J-integral [kJ/m ²]
J_Q	Unclassified (provisional) plane strain fracture toughness
K_I, K	Stress intensity factor [MPa·m ^{0.5}]
MM	Mono-material
P	Load [N]
S	Span between supports [mm]
W	Specimen width [mm]
$Z(BM)$	Position of bi-material dissimilar fusion line, as measured from the same reference plane as a [mm]

Greek symbols

α	BCC phase
α'	BCT phase
Δa	Crack extension [mm]
Δa_Q	Crack extension value at J_Q [mm]
ε	True strain [–]
ϵ	HCP martensite
Γ_J^E	Correction function relating numerical and analytical solutions of J-integral, as a function of reference elastic modulus [kJ/m ²]
Γ_C^E	Correction function relating numerical and analytical solutions of elastic compliance, as a function of reference elastic modulus [kJ/m ²]
ν	Poisson's ratio [–]
σ	True stress [MPa]
Θ	Strain-hardening rate [MPa]

flexibility of WAAM systems to achieve compositional grading and highlight the role of the interface in the overall performance of the bi-material part.

This study concentrates on the combination of austenitic stainless (AS) and high strength low-alloy (HSLA) steels. More specifically, it builds upon our previous work on the microstructural study of a bi-material part obtained by compositionally grading with the wire consumables ER70S-6 and ER316L [9] and its fatigue crack propagation performance [10]. These two consumables are combined with the intention to profit from the virtues of each alloy. The good structural integrity of a HSLA steel coming from an excellent strength and toughness [11] is sought to be complimented by the corrosion resistance [12], ductility, and good performance under cryogenic and high temperature conditions [13] of an austenitic stainless steel. These virtues make this material combination interesting for further study for its wide range of potential applications.

HSLA-AS bi-material steel offers significant advantages for engineering applications. In the petrochemical sector, as noted by Switzer et al. [14], austenitic corrosion-resistant cladding mitigates sulfidation caused by sour crude, while a low-alloy steel backbone provides mechanical integrity at a lower cost. This solution is specifically interesting for pressurized components exposed to acidic environments, such as

tanks and reactors. Similarly, Wang et al. [15] highlighted the maritime industry's reliance on bi-material solutions to enhance the durability and reliability of marine-exposed structural components. The authors mention examples such as boat hulls and ballast water piping, the latter being especially susceptible to corrosion due to seabed ballast water. While traditional cladding methods such as hot rolled bonding, friction welding, and explosive welding are effective manufacturing options for long and flat bi-metal products, they are limited in geometric flexibility. These limitations restrict design innovations that could potentially improve part performance, ease of assembly, and reliability [16]. WAAM offers a viable solution to overcome these limitations by enabling the production of custom geometries. This approach even allows for the fabrication of mechanically loaded components like propellers [17], integrated pressurized vessels [18,19], and other intricate designs that are impractical or cost-prohibitive with alternative methods. As such, additive manufacturing (AM) opens new possibilities for designing high-performance components tailored to demanding engineering environments. However, a clear challenge is to establish adequate reliability levels on the mechanical performance of these components, given the uncertainty derived from the diluted interface layer obtained through dissimilar fusion welding between the two alloys.

Previous work has given indications of the challenges related to combining these two alloys and their effect on the mechanical properties. Under arc-welding processes, the two materials will be diluted by each other in a single weld-pool. The degree of dilution will depend on the deposition parameters. However, the dilution of a chromium-rich austenitic stainless steel onto a ferritic steel consistently leads to the formation of martensite along the fusion line [20], or in the form of martensite islands [21]. Mukherjee and Pal [22] showed that the amount of martensite formed and its effect on mechanical properties will depend on the local chemistry and heat input. Moreover, this alloy combination is susceptible to the formation of Type-II boundaries [23]. They are formed as allotropic transformations at high temperatures result in a matching austenite phase between the dissimilar base metal and the weld metal. These Type-II boundaries may result in poor strength [24], and cracking [25].

As a strategy to address the challenges reported on this dissimilar joint, heat treating has shown mixed results. Ahsan et al. [26] reported important increments in strength and ductility of bi-material specimens by heat-treating their WAAM coupon to 950 °C for 1 h followed by quenching. Nonetheless, the authors contribute this increase in performance to the microstructural refinement obtained at the heat affected zone on the HSLA steel, not to refinement of the microstructure at the interface layer. Longer heat treatments lead to carbon migration from the low alloy steel to the austenite phase across the fusion line [20,27], causing hardness spikes in the austenite alongside ferrite decarburization and softening. Hence, a defect-tolerant approach to the design of these bi-material components might be a necessary alternative to heat treatment.

Useful reference work has been published on the mechanical properties of each individual alloy in the context of WAAM. Both AS and HSLA steel alloys typically show high fracture toughness. On the one hand, Dirisu et al. [28] showed that ER70S-6 yields an average value of $J_Q = 453 \text{ kJ/m}^2$. The superior toughness of this alloy compared to other higher grade HSLA steels is attributed to the refined, non-equiaxed, woven nature of acicular ferrite and the minimal presence of martensite-austenite constituents. These values are consistent with those reported by Ermakova et al. [11] for the same alloy. On the other hand, a large dispersion of values is cited for fracture toughness of AS steel. Kumar et al. [29] reported toughness results for WAAM'ed ER316L to be 160 kJ/m^2 . However, this result suggests lower toughness than previous all-weld tests, with typically reported values between 400 and 450 kJ/m^2 [30,31]. Kumar et al. [29] observed nonetheless that the formation of mechanical twins and eventual fracture is affected by the dislocation structure and grain boundary density of additively manufactured parts. It has been demonstrated that the work hardening mechanism governing the deformation of austenitic alloys with low stacking fault energy (SFE) is dependent on local chemistry, environment, and strain rate [32]. This is an important effect to be considered when discussing the deformation behaviour of a diluted austenitic alloy, such as the interface layer, and for the prediction of the mechanical behaviour of bimetal components.

Considering a defect-tolerant approach to the manufacturing of a AS-HSLA steel component, it is relevant to study the deformation and toughness behaviour of the interface layer in detail. Fracture toughness testing of bi-material specimens conveys nonetheless its own set of challenges. Standard testing specifications require testing specimens to be described through a single elastic modulus [33,34]. Much work has been carried out to further extend the formulations of J-integral to overcome the constraints of elastic homogeneity set by Rice [35] in his original formulation. Jin and Noda [36] postulated solutions for the problem of J-integral formulation across several inhomogeneous situations, including a non-constant elastic modulus along the crack path. Alternative solutions were offered by several authors [37–39], as functional grading became more popular. These solutions rely however on smooth continuous functions of the elastic modulus. A formulation for the J-integral in the vicinity of sharp boundaries between phases was

proposed by Weichert and Schulz [40]. The authors point out that their solution can only be implemented when sharp boundaries are contained within the contour integral considered, making it cumbersome to implement. A practical approach was implemented by Ghorbanpour et al. [41] through finite element analysis. The authors defined a specimen-specific stress-intensity function by using the conventional J-integral formulation at incremental crack extension steps.

Having established the potential benefits and challenges of functional grading through wire arc additive manufacturing, the aim of this work is defined. Through a combination of quasi-static tensile loading, fracture toughness testing, and microstructural evaluation, the fracture toughness and deformation behaviour of the interface layer is to be studied. The results provide evidence on the deformation mechanisms governing the plastic strain and final fracture. Complimentary FEM analysis is implemented to bridge the gap between the available standard procedure of fracture toughness testing and the specific requirements set by testing non-isotropic specimens.

2. Materials and method

2.1. Wire arc additive manufacturing and consumables

To obtain the specimens necessary for mechanical testing, a functionally graded block and two complimentary mono-material blocks were additively manufactured using WAAM. All blocks had approximate dimensions of $210 \times 90 \times 60 \text{ mm}$ and were built on a low-alloy high strength steel plate substrate. The wire consumables selected were 3Dprint AM 46 and 3Dprint AM 316L from Böhler Voestalpine of 1.2 mm diameter. These alloys are specifically designed for additive manufacturing, while still complying with the AWS chemical specifications for ER70S-6 [42] and ER316L [43] respectively. The chemical compositions of the wires as stated by the manufacturer are presented in Table 1. The bi-material block was produced with a Fronius CMT power source combined with a Fanuc M710iC/12 L series robot, as shown in Fig. 1 (a). The work piece was clamped at 4 points during the entire AM process. An Infratec VarioCAM HD thermal camera and Irbis 3 software were used to monitor the interpass temperature of the block.

The mono-material and bi-material blocks were manufactured with similar specifications. The bi-material block consists of 16 layers of ER70S-6 followed by 16 layers of ER16L. The layers of ER70S-6 comprised of 15 beads per layer, with a distance of 4 mm between bead centres. This pattern yields about 25 % overlap between beads and an average layer height of 3.5 mm. All beads in a layer were deposited in the same orientation; for the subsequent layer, the deposition orientation was reversed. When all 16 layers were deposited, the block was unclamped and machined flat at an average depth of 2.5 mm from the top surface. This was done to minimize geometrical deviations due to material build-up in the start-stop regions. On the machined surface, ER316L was deposited in layers consisting of 13 beads per layer, at 4.6 mm between bead centrelines. With these deposition parameters, each layer would reach about 2.5 mm height and while a 25 % bead overlap was maintained. The welding parameters used for each consumable are presented in Table 2, alongside the calculated heat input. A mixture of Ar20He12CO2 shielding gas was used for the ER70S-6 wire whereas a mixture of Ar35He2CO2 was used for the ER316L each with a flow rate of 15 L/min. The complimentary mono-material blocks were also

Table 1
Chemical composition of wire consumables selected, as stated by the manufacturer in wt% [44,45].

	C	Si	Mn	Cr	Ni	Mo	N	Fe
3Dprint AM 46 (ER70S-6)	0.1	1.0	1.7	–	–	–	–	bal.
3Dprint AM 316L (ER316L)	0.015	0.45	1.6	18.5	12.0	2.5	0.04	bal.

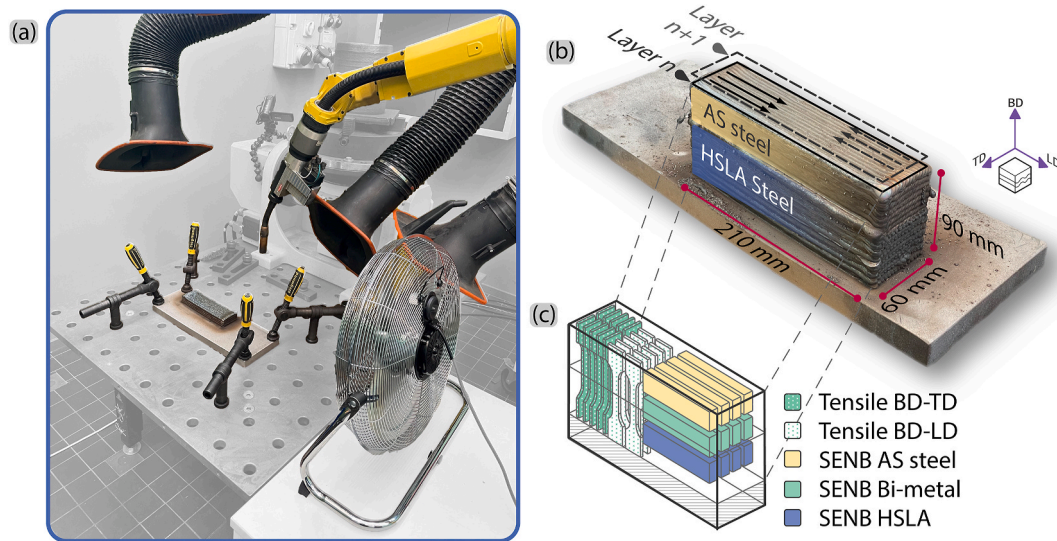


Fig. 1. (a) Wire arc additive manufacturing setup, (b) bi-material block with schematic of building strategy and (c) schematic indicating approximate specimen orientation and location within bi-material block.

Table 2

Target voltage (U), current (I), wire feed speed (WFS), travel speed (TS), contact tip work distance (CTWD), heat input (HI) and interpass temperature for each material used through the additive manufacturing process.

	Welding Mode	Target U	Target I	WFS	TS	CTWD	HI	Int. Temp.
		V	A	m/min	mm/s	mm	kJ/mm	°C
HSLA steel 3Dprint AM 46	CMT	21.1	143	7.5	10	17	0.27	80–140
AS steel 3Dprint AM 316L	P-CMT	13.2	214	5.0	10	17	0.22	80–140

additively manufactured with these parameters.

2.2. Tensile testing and in-situ digital image correlation

To evaluate the mechanical properties of both mono-material and the bi-material blocks, quasi-static tensile testing was conducted. Four sets of tensile specimens were manufactured for this purpose. The first two sets consisted of bi-material specimens extracted from two plane orientations along the build direction (BD), as illustrated in Fig. 1 (c). These orientations were chosen to assess the effects of strain concentration caused by the geometry of the interface layer. Dog-bone specimens were extracted from flat slabs with a thickness of 3 ± 0.02 mm. The final shape was achieved through waterjet cutting, featuring a constant width of 6 ± 0.03 mm and a gauge length of 35 ± 0.15 mm. The surface quality was maintained as obtained by machining operations. The remaining two sets of specimens were extracted from mono-material blocks with similar dimensions to those depicted in Fig. 1 and deposition parameters detailed in Table 2. The specimens were machined and turned to obtain a cylindrical cross-section of $\varnothing 6 \pm 0.03$ mm along a gauge length of 35 ± 0.15 mm.

Tensile testing was carried out using a Zwick Z100 universal testing rig operating under crosshead displacement control. Load was measured with a cell rated for 100 kN. The test was performed at a displacement rate of 0.005 mm s^{-1} under ambient conditions. The zero-point setting, gripping, and post-mortem calculations were conducted in accordance with EN-ISO 6892-1:2019 [46]. For mono-material specimens, strain measurements up to 5 % were obtained using a clip-on Zwick Digiclip extensometer with a 20 mm gauge length; beyond this strain value, the extensometer was removed, and strain was derived from an adjusted crosshead displacement. For bi-material specimens, strain was measured through digital image correlation (DIC) around the interface layer. A

commercial LIMESS Q400-3D stereo camera system was employed for this purpose, featuring a 40 mm focal length and a 5 MPixel camera sensor operating at a 0.5 Hz acquisition rate. Specimen surfaces were prepared with speckle patterns using aerosol paint. The captured images were post-processed using LIMESS ISTR 4D software. Tensile stress-strain curves were obtained by measuring local engineering strain along the interface by an average of five parallel digital strain gauge lines.

2.3. Fracture toughness measurements

Fracture toughness measurements were carried out using SENB specimens subjected to three-point bending, following the specifications set by the relevant ASTM standard [34]. The specimens were machined from the bi-material block at the locations indicated in Fig. 1 (c). Cutting and machining operations to extract testing specimens generally relieves the material, especially if the specimen is small compared to their parent part (Jiang et al., 2013). Specimens are thus designed as small as possible to benefit from stress relaxation. Specimens had a width (W) of 20 mm and a thickness (B) of 10 mm. Bi-material specimens were machined in such way such that the interface layer can be found at a position $Z(BM)/W$ ranging between 0.45 and 0.6. Roller pin supports of $\varnothing 12$ mm were set at 80 mm centre-to-centre distance to conform with standard specifications. A starting notch of 0.4 mm width was created on each specimen using electrical discharge machining (EDM) to a depth of 3 mm. Specimen pre-fatigue was performed from a starting ΔK of $25.3 \text{ MPa}\cdot\text{m}^{0.5}$, reduced every 0.5 mm of crack extension down to $12.7 \text{ MPa}\cdot\text{m}^{0.5}$, until the pre-fatigue crack reached a length of 9 mm. This procedure followed an exponentially decreasing ΔK -gradient C : 0.23 mm^{-1} by increasing K_{\min} . Pre-fatigue crack length was monitored visually with position markings on the specimens' side faces. After

pre-fatiguing, side-grooving was performed on all specimens to obtain a reduced thickness of B_n of 8 ± 0.03 mm. An illustration of a specimen and key elements of the experimental setup are depicted in Fig. 2.

As mostly stable tearing is expected, the testing procedure follows the process to construct R-curves from single specimens. For this purpose, an Instron Electroplus E20000 testing bench was used and controlled with the Bluehill Fracture software. Load was measured with a cell suitable for ± 15 kN. Specimens were loaded under displacement control at a consistent rate of $0.2 \text{ mm}\cdot\text{min}^{-1}$, typically reaching the target load P_m within 40–50 s. Load-unload cycles were employed every $50 \mu\text{m}$ of crack mouth opening displacement (CMOD), with an unloading range of 1 kN and no hold time. CMOD was recorded using an Epsilon 3541 clip-on gauge extensometer with a 3 mm gauge length and a maximum extension of 2.5 mm. The gauge was attached to the specimen via detachable knife edges, secured with screws tightened onto the specimen's surface. Since the tip of the clip-on COD gauge was positioned 2 mm above the specimen surface, adjustments to the CMOD readings were necessary following NEN-ISO 12135:2021 [33].

Special considerations were made to derive the crack-length extension measurements. For mono-material specimens, this parameter was estimated from the CMOD compliance through established standard relationships [33,34]. Nevertheless, a special case is considered for the bi-material specimens. To account for the sharp change in elastic modulus, the elastic compliance is corrected proportionally by the results obtained through FEM.

2.3.1. Special considerations for J_{el} and elastic compliance of a bi-material SENB specimen

Standardized test procedures provide a framework to reliably obtain comparable material properties. However, international standards do not foresee testing bi-material specimens for fracture toughness. This is especially relevant when considering a bi-material specimen with heterogeneous elastic properties. Additional considerations are required to capture the interface effect of a bi-material specimen. To bridge the dependency of standard testing procedures on a single elastic modulus E , a numerical approach is used. This is done following the procedure proposed by Ghorbanpour [47] for functionally-graded SENB specimens. A linear-elastic Finite Element Analysis of a bi-material specimen was used to capture the effect on J_{el} and elastic compliance. This FEM model definition and result analysis is explained in detail in Annex B. In short, a solution space for J_{el} and the elastic compliance are obtained by varying the length of a modelled crack a , and the position of the bi-material interface layer $Z(BM)$. Correction functions are used to capture the difference between the numerical results and the analytical expressions available in standard testing procedures. These functions are later used to translate the experimentally captured data into results

useful for analysis of a bi-material specimen. The first correction function is defined as follows:

$$\Gamma_J^E = \frac{J_{el,FEM,BM}}{G_{Analyt,MM}^E} \quad (\text{Eq. 1})$$

where $J_{el,FEM,BM}$ is the FEM solution of the elastic component of J -integral for a bi-material specimen and $G_{Analyt,MM}^E$ is the analytical description of elastic energy per unit area of crack extension for a mono material specimen with elastic modulus E . A superscript E denotes that this function definition depends on the reference value of elastic modulus E used. The function is used to determine $J_{el(i)}$ for bi-material specimen, such that:

$$J_{el(i)} = \Gamma_J^E \cdot \frac{K_{(i)}^2 \cdot (1 - \nu^2)}{E} \quad (\text{Eq. 2})$$

where $K_{(i)}$ is the stress intensity factor, which is in turn dependent on the load, geometry of the specimen and crack length. In this case, ν is the Poisson's ratio. The subscript (i) is used to indicate a load-reload cycle in the single-specimen fracture toughness test procedure.

The second function bridges the difference between the mono-material and the bi-material specimen compliance. Given that CMOD measurements are used to estimate the crack length during testing, it is necessary to later derive the crack extension values per load-unload cycle Δa . This function is defined as follows:

$$\Gamma_C^E = e_{a/W} \cdot \frac{C(a/W)_{FEM,BM}}{C(a/W)_{Analyt,MM}^E} \quad (\text{Eq. 3})$$

where $C(a/W)$ is the function that relates crack length for a SENB specimen and the CMOD-load compliance. The function $e_{a/W}$ describes inverse of the fitted error function encountered between the analytical and numerical compliance values for mono-material specimens. This function is explained in detail on Eq. (C1) through C3 in Annex C. The subscript FEM, BM denotes the a/W values are obtained through FEM modelling of a bi-material specimen, and the subscript $Analyt, MM$ indicates the a/W values obtained from the analytical expression presented on Eq. (B6) in Annex B. The compliance relationship between presented in Eq. (C1) in Annex C and the correction function Γ_C^E are used to predict the crack size during testing through the following relationship:

$$C(a/W)_{BM,(i)} = \Gamma_C^E \cdot C(a/W)_{Analyt,MM,(i)}^E \quad (\text{Eq. 4})$$

Note that the solution of $C(a/W)$ is dependent on the elastic modulus of the material at which the crack front is found. This modification is sufficient to evaluate the relationship between the specimen compliance and the crack length for every i -th load-unload cycle using the standard procedures.

2.4. Fractographic analysis

To carry out the post-mortem inspection, the tested SENB specimens were cracked open under cryogenic conditions. To avoid corrosion of the fracture surface caused by de-icing, the cracked specimens were warmed up in water at room temperature, followed by a short submersion in isopropanol and final drying in air. The AS steel mono-material specimens were heat-stained at $370 \text{ }^\circ\text{C}$ for 15 min and left to cool down to room temperature and cracked open thereafter.

Macroscopic characterization was carried out with a VHX-7000N Keyence digital microscope equipped with optical shadow effect mode. Microscopic characterization was carried out with a Thermo Fisher Helios G4 PFIB UXE Dual Beam Microscope. Images were obtained with an ETD secondary electron detector at an accelerating voltage of 10 kV.

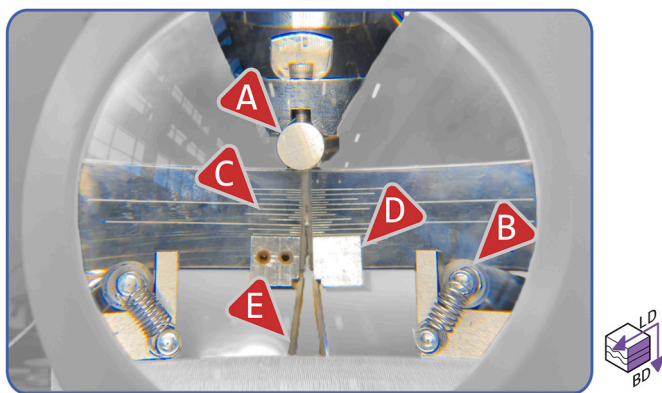


Fig. 2. Experimental fracture toughness set-up. Markers highlight bend-test fixtures (A and B), pre-fatigued and grooved SENB specimen with 0.5 mm markings (C), demountable knife edges (D), and legs of the attached clip-on crack opening displacement (COD) gauge (E).

2.5. Crystallographic analysis

SENB specimens were used for crystallography characterization at the crack flanks by means of electron back-scatter diffraction (EBSD). The surfaces mapped coincide with the longitudinal centreline of each specimen. Standard metallographic preparation included sanding up to #2000 paper grit, polishing with 0.3 μm and 0.1 μm diamond suspensions, and a final step of polishing with an active oxide suspension (OPS).

The camera and software used for crystallographic mapping were proprietary of AMETEK EDAX integrated into the Thermo Fischer Helios equipment. Mapping was done under 15 kV accelerating voltage and a current of 13 nA. Step size was adjusted depending on the size of the region of interest and it is indicated on the caption under each map shown in the results and discussion sections. Inverse Pole Figure (IPF) maps are shown with $\langle 001 \rangle \parallel \text{BD}$. Clean-up was done cautiously to avoid incurring in large biases: Neighbour orientation correlation with a grain tolerance angle of 5° was used to clear points with a confidence index lower than 01. Kernel average misorientation (KAM) values were

obtained for the 1st nearest neighbour with a maximum misorientation of 5° . Grain boundary texture was calculated as a harmonic series expansion of rank 16, with a Gaussian half-width of 5° and misorientation boundaries between 5° and 180° . The grain boundary misorientation distribution function (MDF) encompasses a $[0^\circ-65^\circ]$ misorientation range, $[0^\circ-45^\circ]$ azimuthal range, and a $[0^\circ-55^\circ]$ polar range. Only correlated MDF values were considered.

3. Results

3.1. Tensile testing and in-situ digital image correlation

To investigate the effect of dilution at the interface layer, digital image correlation (DIC) is used to measure deformation during quasi-static tensile loading. The results are useful to describe two specific phenomena: the elastic behaviour and the work-hardening behaviour of the bi-material interface. The former is necessary for the description of the stress concentration effect in a bi-material 3-point bending SENB specimen. The latter is used to describe the effect of dilution on the

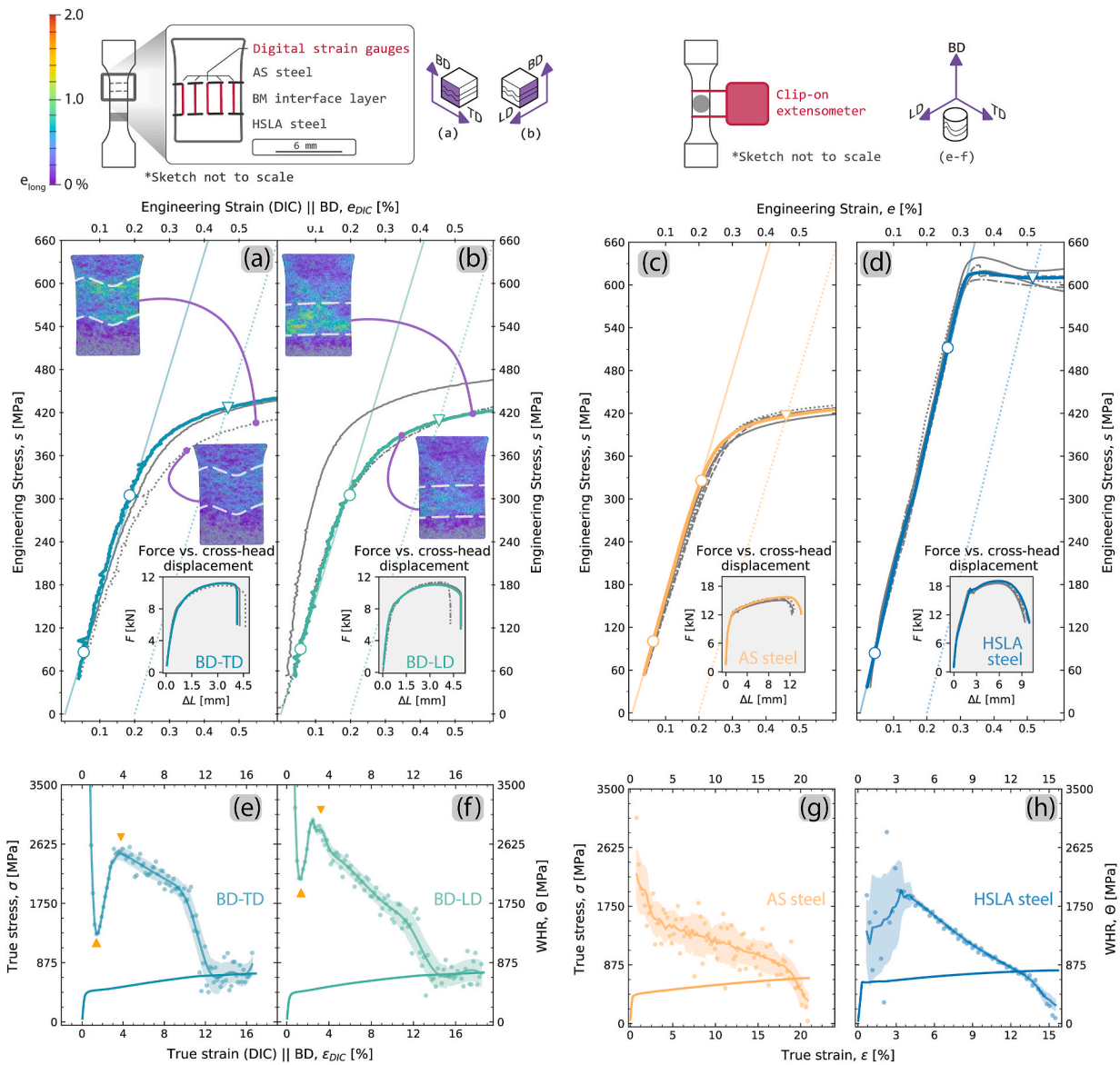


Fig. 3. Elastic modulus and yield behaviour as obtained through DIC measurements for (a) BD-TD and (b) BD-LD bi-material sample groups, and as obtained through physical strain gauge measurements for (c) AS steel and (d) HSLA steel specimens. The yield values are obtained through a 0.2 % intercept proof strength. An example of true-strain, true stress and work-hardening rates are shown for (e) BD-TD and (f) BD-LD specimens, and (g) AS steel and (h) HSLA steel specimens.

work-hardening mechanisms of the interface layer.

The elastic portion and early yielding stages of the quasi-static tensile curves are presented on Fig. 3. The figure shows the engineering stress-strain relationship measured on the plane formed between the build and transverse direction (BD-TD) in Fig. 3 (a), and the build and longitudinal direction (BD-LD) in Fig. 3 (b). For comparison, stress-strain relationships are provided for AS and HSLA steel mono-material specimens on Fig. 3 (c) and (d) respectively. In favour of clarity, the strain-stress relationship of a representative specimen is plotted in colour per orientation, while test repetitions are shown in grey. For the two chosen specimens, corresponding DIC maps are shown along the line for the indicated load levels.

Despite the overall similarity in tensile response of all measured specimens, a clear distinction is observed through strain localization. This difference is made evident through the DIC map insets. Strain maps are shown at two strain levels for each plane measured in Fig. 3 (a–b). Strain partitioning is observed at the fusion lines between the different materials volumes for the specimens mapped in the BD-TD plane. Given an averaged 0.55 % engineering strain, local values register 1.2 % strain localized at the fusion lines bounding the diluted interface layer. This comes in contrast with the centre of the specimen, where values are registered to match with the bulk behaviour. For the BD-LD plane, the specimens display a clearly different behaviour with regards of strain partitioning. At an engineering strain level of 0.55 %, the mapped surface shows shear banding. These bands extend through the fusion line between the interface layer and the AS steel material volume. Despite the differences in localized strain, the averaged elastic modulus measured across the diluted interface is consistent on both planes. The most relevant quasi-static properties derived from these results are presented in Table 3.

True stress-true strain relationships and work-hardening rates are shown on in Fig. 3 (e) and Fig. 3 (f). A detailed elaboration on the auxiliary relationships used to obtain these values and the computation of the average line and error bands are explained in Annex A. The work-hardening rate (WHR) shows a non-linear relationship with respect to true strain ϵ . This relationship is shown in Fig. 3 (e) and Fig. 3 (f), contrasting with the WHR behaviour of both AS and HSLA steels shown in (g) and (h). The data shows a valley within $\epsilon < 2$ %, followed by a subsequent crest, regardless of the orientation of the specimen measured. The position of the crest typically lies between $3 \% < \epsilon < 4.5$ %. Values of WHR measured at the crest vary substantially, yielding $\Theta = 2255$ MPa with a standard deviation of 433 MPa if both specimen orientations are considered. Notwithstanding the variability of results, the overall trend remains consistent: an assisting work-hardening mechanism controls the plastic deformation of the diluted interface layer, different from that of the undiluted material. For metastable austenitic stainless steels, this observation has been associated with either twinning induced plasticity (TWIP) or transformation induced plasticity (TRIP) effect, depending on the local chemistry and temperature. This is

Table 3
Mechanical properties for the bi-material interface and undiluted WAAM'ed AS and HSLA steels.

	Elastic Modulus E	Yield Strength $s_{0.2}$	Tensile Strength s_u	Avg. strain-hardening exponent n
	GPa	MPa	MPa	log(MPa)
Mono-material AS steel	154 ±8	418 ±5	548 ±4	0.197 ±0.011
Diluted interface	157 ±17	412 ±13	592 ±11	0.210 ±0.020
Mono-material HSLA steel	197 ±6	608 ±7	683 ±9	0.122 ±0.009

addressed in detail in section 4.

3.2. Fracture toughness and R-curve determination

Fracture toughness testing on both mono-material and bi-material SENB specimens adhered to the established standards [34]. This section presents the results obtained from single-specimen testing methodology. A standard procedure was followed for mono-material specimens. The formulations presented on the previous section are used to correct the standard analytical solutions for the specific case of a bi-material specimen.

The load-CMOD curves for all test specimens are presented on Fig. 4. Fig. 4 (a) and Fig. 4 (b) show mono-material results, highlighting the load-displacement behaviour of a specimen arbitrarily chosen. Fig. 4 (c) shows the load-CMOD values for bi-material specimens. Each bi-material specimen is identified individually with labels BM-A through BM-D to easily correlate the resistance curve (R-curve) results and features found through fractography and crystallography. For each specimen presented, coloured highlighting is used to denote different material volumes through which the crack extends; yellow highlighting denotes undiluted AS steel, whilst blue indicates HSLA steel. The bare green line is thus the domain of interest, as it denotes the diluted interface layer.

Using the results obtained from the load-CMOD curves, it is possible to construct the resistance curves for the specimens tested. For mono-material specimens, the standard relationships to obtain J and Δa [34] are used. The R-curves of these specimen groups are shown in Fig. 5 (a) and Fig. 5 (b) for the AS steel and the HSLA steel. The numerical results for J_Q , Δa_Q , and proposed values for J_{IC} are tabulated in Table 4. Benchmark reference values are provided compare the obtained J_{IC} values with comparable literature.

Fig. 5 (c) presents the R-curves taking into consideration the relationships established by Eq. (2) and Eq. (4). The results are presented with a slight modification: all values of Δa are shown relative to the position of the bi-material interface $Z(BM)$. This is done to highlight the similarities in the $J - \Delta a$ given each material domain, and discriminate the differences caused by the position of the initial crack length a_0 . The inset in this figure presents the R-curves without such modification for the specimens BM-B and BM-D. These specimens were chosen, as they comply with the minimum number of valid $J - \Delta a$ data pairs necessary for determination of J_Q obtained solely along diluted interface. The points circled on the main plot for ease of identification.

The position of a_0 at the start of the test has a clear effect on the values of J for bi-material specimens. As mentioned before, specimen BM-A in Fig. 5 (c) shows the special condition, where a_0 lies within the material domain of AS steel. For the nine Δa increments registered within this domain, a larger accumulated value of J is obtained. This result gives an indication of the behaviour of a bimetal part but conveys biased values of J if the behavior of the diluted interface is to be quantified. For the rest of the specimens, more points become available for statistical analysis as the value of $Z(BM) - a_0$ increases. This also conveys in turn higher values of J_{el} when the crack crosses the dissimilar fusion line.

The R-curves shown in Fig. 5 reveal important specimen-specific differences between the diluted interface layer and its surroundings. Except for specimen BM-A, a drop of J is observed at the position where $\Delta a = a_0 - Z(BM)$ for every bimetal specimen. Also, specimens BM-A through BM-C display locations where large increments of Δa were measured for small corresponding increments of J . Both specimens BM-A and BM-B show one of these large Δa steps within the last 0.5 mm ahead the dissimilar fusion line between the interface layer and the HSLA steel. This observation exemplifies the variability in crack-propagation behaviour across the interface layer.

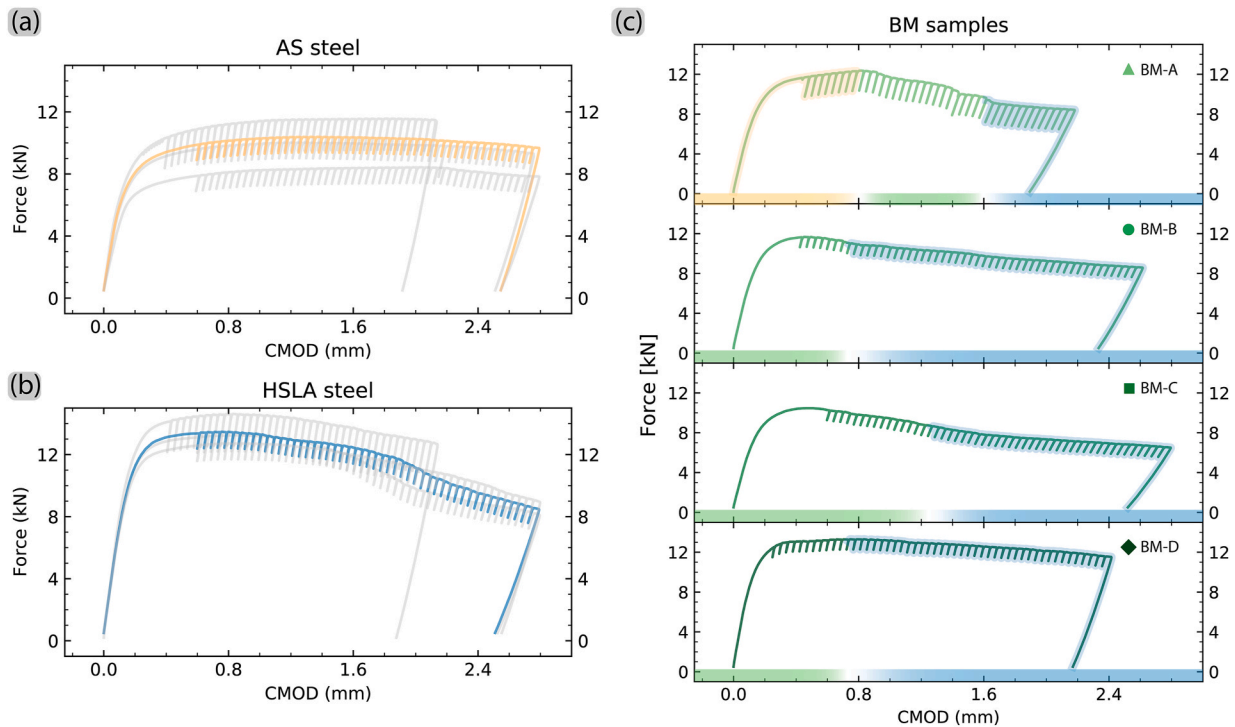


Fig. 4. CMOD vs. force curves for mono-material (a) AS steel, (b) HSLA steel, and for (c) bi-material specimens. For (a) and (b), repetition tests are shown in grey. In (c), yellow highlights the load-unload cycles where the crack front is estimated to lie within the undiluted AS steel, blue highlights those cycles within HSLA steel, and the bare green line represents the diluted interface layer.

3.3. Post-mortem inspection of the fracture surface

Fractographic inspection is used to determine relevant geometrical and fracture features. Fig. 6 shows the location of a_0 , a_p , and $Z(BM)$ for selected specimens. With exception of specimen BM-A, a_0 resides within the material volume of the diluted interface layer as shown in Fig. 6 (a–c). Considerable variations of the initial a_0 and final a_p crack positions are observed. This is true not only for the bi-material specimens, but also for the AS steel specimens shown in Fig. 6 (d–f) and the HSLA steel specimens shown in Fig. 6 (g–i). These deviations are evaluated against a limiting deviation value of $0.1 \cdot (b_0 \cdot B_n)^{1/2}$ as detailed in the standard test method [34]. Specimens that did not comply with this criterion were excluded from statistical considerations of J_{IC} cited on Table 4.

Alongside the position and geometry of the crack front at a_0 and a_p , distinct macroscopic fracture structures are observed. On Fig. 6 (a), markers A, B and C indicate the zones corresponding to pre-fatigue, stable tearing, and final fracture. The pre-fatigued zone shows a faceted fracture surface obtained across the AS steel. This topography changes at a_0 , where the driving crack propagation behaviour changes from fatigue to steady tear. The small regions of undiluted AS steel and HSLA steel deformed by steady tear show a very similar topographic character than that of the mono-material specimens. There, the corresponding fracture surfaces show indications of ridges and large plastic deformation obtained by tearing. By comparison, the region belonging to the diluted bi-material interface shows a less faceted fracture surface than that of the undiluted counterparts. However, a feature common to all bi-material specimens is indicated by marker D. At this location, the fusion line between the diluted interface layer and the HSLA steel is outlined by a small region which shows signs of low deformation capacity.

A few relevant microscopic fracture features obtained from the bi-material specimens are presented on Fig. 7. Fig. 7 (a–d) show typical traits as obtained through the stable tearing process, including detail areas for the undiluted AS steel in Fig. 7 (b), the diluted interface layer in

Fig. 7 (c) and HSLA steel in Fig. 7 (d). Both the AS steel and the diluted interface layer fracture surfaces show dimple diameters within the range of a couple of microns, although dimple sizes appear to be marginally larger in the diluted material. In both cases, second phase particles inhabit many of the dimples pictured, suggesting a coupled void nucleation effect during the early tearing process. Fig. 7 (c) shows with red markers disperse locations of quasi-cleavage fracture. Fig. 7 (d) on the other hand shows a large band of quasi-cleavage fracture alongside the dissimilar fusion line, matching the features observed under macroscopic inspection. This region matches that of the martensite obtained during solidification, hereon referred to as allotropic martensite. Enlarged dimples in varying directions and secondary crack features about $Z(BM)$ are shown in both Fig. 7 (a) and (d). These suggest complex tearing interactions leading to the fracture of this material volume.

Continuing with the microscopic fractography, Fig. 7 (e–f) present traits that suggest sources of low local tear resistance. Marker A on Fig. 7 (e) shows an alternative location of a band of quasi-cleavage fracture, like that at $Z(BM)$. This band is nevertheless not commonly found elsewhere. Additional features include the brittle deformation structures occasionally observed at the bead roots of the diluted interface layer. These are pointed by markers D in Fig. 7 (f) and marker E on Fig. 7 (g), as found on specimens BM-D and BM-A correspondingly. A combination of ductile and cleavage fracture is observed in the depth of these faults, suggesting a complex interaction of several different local structures. An additional example of secondary cracking is pointed by marker C. This last feature is fully populated by dimple structures, showing otherwise no signs of brittle deformation.

3.4. EBSD mapping of fracture profile

The investigation of the fracture surface through microscopy provides detailed information of the stable tearing process. Nonetheless, plastic deformation can largely dissipate strain energy and restrict crack extension. To understand the plastic deformation mechanisms, it is useful to study the crack flanks and their microstructural features. A

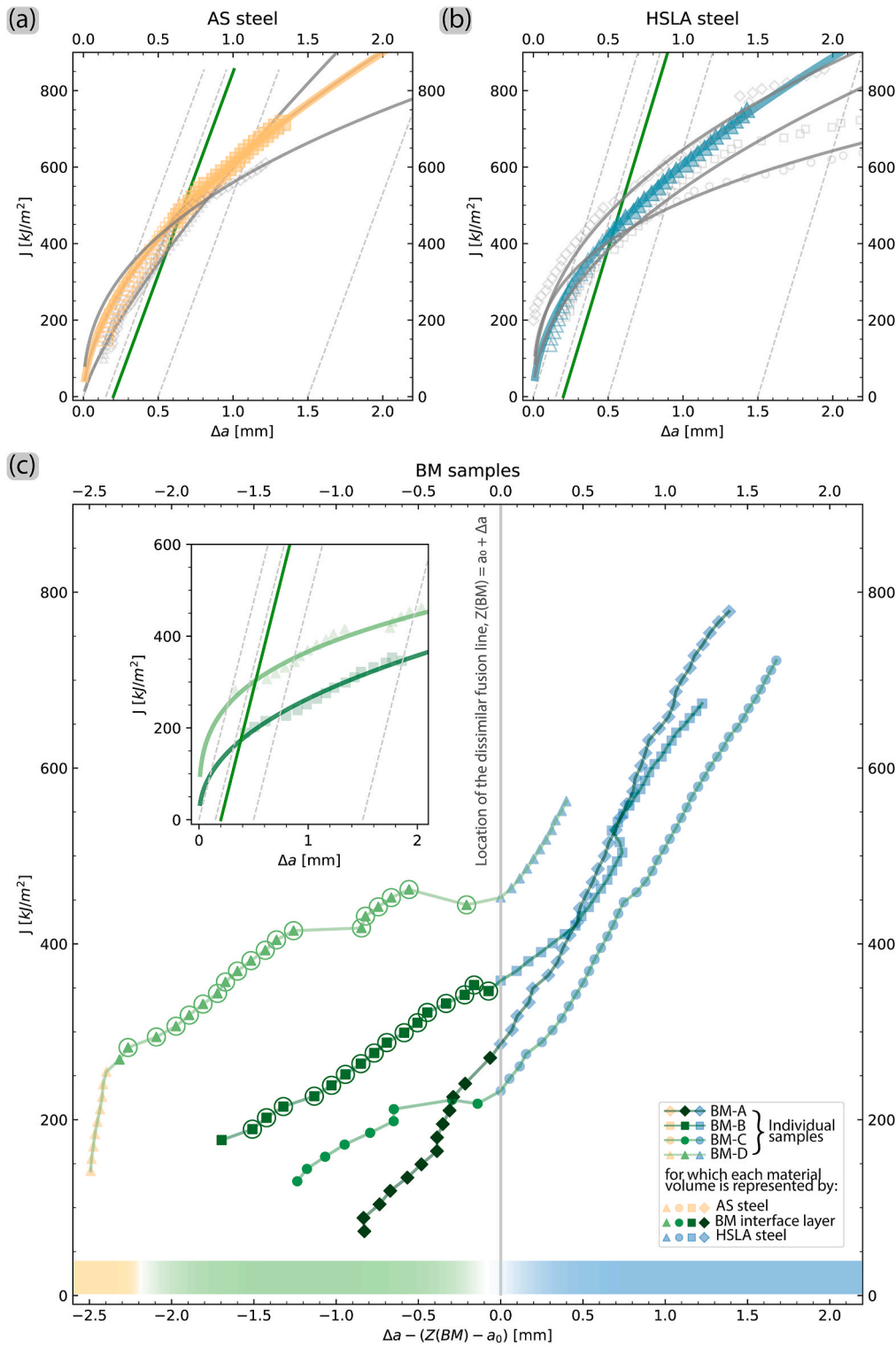


Fig. 5. Representative R-curves for (a) AS steel specimens and (b) HSLA steel specimens, with valid data-pairs available for regression shown as filled markers. Repetition test shown in grey. (c) Bi-material specimens R-curves plotted relative to the position of the bi-material fusion line. Data points qualifying for further J_Q analysis are circled and shown in inset with corresponding exponential regression results.

related study [9] shows that the chemistry and microstructure at the interface better resemble those of an austenitic stainless steel alloy and less so to those of a HSLA steel alloy. A comparative benchmark is thus provided in detail for the former alloy to easily discuss the peculiarities of the interface layer. For this, EBSD mapping is utilized. For the latter alloy, the reader is referred to the study of Costin et al. [50], which provides an in-depth analysis of deformation mechanisms during

fracture of acicular ferrite.

The crack flanks of a mono-material AS steel specimen are studied as a baseline reference. This is done to compare how plastic strain is accommodated for this material volume in an undiluted condition. Fig. 8 (a) shows a low-magnification IPF map. The map is composed by IPF orientation mapping with a grey-scale overlay of the Image Quality (IQ) values. The IQ greyscale overlay is used to highlight defects on crystal

Table 4

Overview of fracture toughness results. Error values are defined as \pm one standard deviation.

Sample group	J_Q	Δa_Q	J_{IC}	Literature reported J_{IC}
	kJ/m ²	mm	kJ/m ²	kJ/m ²
AS Steel	463 \pm 57	0.66 \pm 0.07	459 \pm 69	400-450 ^b
Bi-material	236 \pm 78	0.46 \pm 0.06	180 ^a	–
HSLA steel	436 \pm 59	0.54 \pm 0.05	408 \pm 26	420 \pm 73 ^c

^a Result obtained from a single valid specimen.

^b All-weld GMAW or GTAW metal as reported by different sources [30,48].

^c [11,49].

lattice, such as grain boundaries and regions of high dislocation density. Assuming adequate sample preparation and indexing parameters, shear bands, twin boundaries, as well as martensite characteristically show low indexing values as well.

Detailed mapping for the pre-fatigue and the steady tear crack flank domains are provided on Fig. 8 (b–d) and Fig. 8 (e–g). At each location IPF, KAM and phase maps are included. The location of the crack flank presented on Fig. 8 (b–d) shows minimal lattice misorientation within individual grains. This indication of low deformation is accompanied by low first-neighbour KAM values, and a typical FCC fraction for this welding consumable. These values contrast with the location of the crack flank presented on Fig. 8 (e–g). There, high lattice rotations within the deformed grains are found, alongside high KAM values, suggesting a high density of geometrically necessary dislocations. At a_0 , a dense network of shear bands is appreciated. The density of shear bands as well as the KAM values decrease in the lower portion of the map. Within the region mapped the FCC fraction remains constant, nonetheless, indicating that the dominant deformation mechanism does not include the transformation of austenite into α' martensite under the chosen testing conditions. It is useful to note that the first value of Δa for this specimen is estimated to be 146 μ m; the second load-unload cycle is expected to be located out of range beneath the region mapped.

Having established a baseline of values and identified some deformation mechanisms in the undiluted AS steel, it is possible to characterize by comparison those traits found in the diluted interface layer. The crack flanks of a bi-material specimen are mapped on Fig. 9. Fig. 9 (a) shows a low-magnification IPF mapping of both crack flanks. Following the same representation method, image quality maps are superimposed as greyscale. On this occasion, martensite bands are identified along the lower region of the diluted interface layer. They are pointed by the red markers on the left flank, although they may be found on either side of the crack. They are confirmed to be martensite by inspection of their morphology in un-deformed regions and are considered to originate from the local chemistry when the diluted layer solidified. For this reason, due to the high content of ferrite and martensite phase fractions in the region mapped, IQ cannot be attributed to the deformation of the crystal lattice.

A detailed map of the region where the crack flank and this martensite band converge is shown under higher resolution on Fig. 9 (c–e). Although a clear distinction cannot be made between α' and α through this indexing method due to the minute differences between both lattice parameters, the lath packaging morphology of martensite is clearly apparent on Fig. 9 (c). Also, Fig. 9 (e) indicates that only a small portion of this region of interest is retained austenite. This detail belongs to a volume fraction that cannot accommodate large plastic deformation, as confirmed by geometry of the crack flanks surrounding this region. This is visible, as the adjacent material above and below shows large deformation into the crack plane.

It is the case that a_0 lies within the diluted interface layer in this specimen and section plane observed. This location develops large amounts of plastic strain to accommodate crack blunting and eventual crack extension. To distinguish the effect of different levels of strain imposed on the microstructure, it is useful to study the features observed

as a function of distance from the crack flank. Detailed maps have been set at 0, 200, 400 and 800 μ m for this purpose. The specific locations of these maps are shown on Fig. 9 (b).

A distinction between allotropic martensite and that obtained through large deformation is required. Directly on the crack flank, Fig. 9 (f–h) shows the effect of the largest expected strain acting about the crack front. Like the microstructure found at the dissimilar fusion line, the crack flank at this location is mostly populated by martensite. This is identified by its morphology, high KAM values and primarily BCC phase indexation. However, the KAM values and the fraction of FCC for the region of interest indicated in both Fig. 9 (g) and (h) suggest a fundamental difference between this location and the one adjacent to the dissimilar fusion line Fig. 9 (c) and Fig. 9 (d). The KAM values of martensite are not expected to increase due to plastic strain, and KAM values obtained from allotropic martensite are measured at about 0.8°. Thus, the martensite observed in Fig. 9 (f) is considered to originate in large from a different driving force, namely, the strain-induced transformation of metastable austenite.

At more distant positions away the crack plane and into the crack flank, the distinction of martensite becomes less straightforward. The morphology of the BCC grains as observed on Fig. 9 (i–o) does not suggest clear martensitic characteristics. Nevertheless, FCC fraction appears to increase as a function of distance, and KAM values gradually decrease. Both these values are indicated for the maps on Fig. 9 (j–p) and Fig. 9 (k–q). These values provide an indirect quantitative measure derived from the mechanisms accommodating plastic strain.

4. Discussion

4.1. Accounting for bi-material interface in fracture toughness testing

The effect of a sharp change in E-modulus across the bi-material interface has a clear impact in the numerical solution of J-integral. As the solution for J_{el} on a bi-material specimen is demonstrably discontinuous, the numeric correction factor Γ_J^E introduces a discontinuity as well. The effect is made apparent when the elastic and plastic components of the experimentally obtained J-integral are compared. This is done on Fig. 10, where (J_{el} , J_{pl}) data pairs are plotted. Fig. 10 (a) and (c) show continuous functions for the values obtained from the AS steel and the HSLA specimens. Nonetheless, the non-continuous relationship between relative crack length a/W and Γ_J^E for bi-material specimens leads to a sudden drop in the estimated J_{el} . This relationship is shown in Fig. 10 (b). Given the specimen geometry, pre-crack length and loading conditions of the method chosen, this drop accounts for about 15–19 kJ/m² of elastic energy, or between 4 and 7 % of the total J value measured at the position where $a = Z(BM)$.

Although a discontinuity is observed in the function describing J_{el} , the relationship that describes the crack length as a function of compliance shows to be continuous. Data points relating these two values are presented on Fig. 10 (d–f). The effect that the bi-material interface has on the elastic compliance curves is that each curve is offset from the others. Consequentially, larger values of $Z(BM)$ entail that the specimen becomes less stiff and thus more compliant in the presence of a crack. This has in turn a small effect on the evaluation of crack length. For example, given the specimens BM-B and BM-C under the same measured CMOD compliance of $2.0 \cdot 10^{-8}$ N/mm, a difference in position of $Z(BM)$ of 1.27 mm yields a difference of estimated crack length of 0.244 mm, or about 2.4 % relative error.

Alongside the intricacies derived from the mathematical description of J, other testing difficulties arise while trying to obtain and interpret data adequately. In terms of the pre-fatigue process, it is a non-trivial task to accurately estimate the crack depth before the fracture toughness test is completed. This opens the possibility to start the test within an unintended material domain. Such is the case for specimen BM-A. Pre-fatiguing the sample up to an unnecessarily long crack leads to a

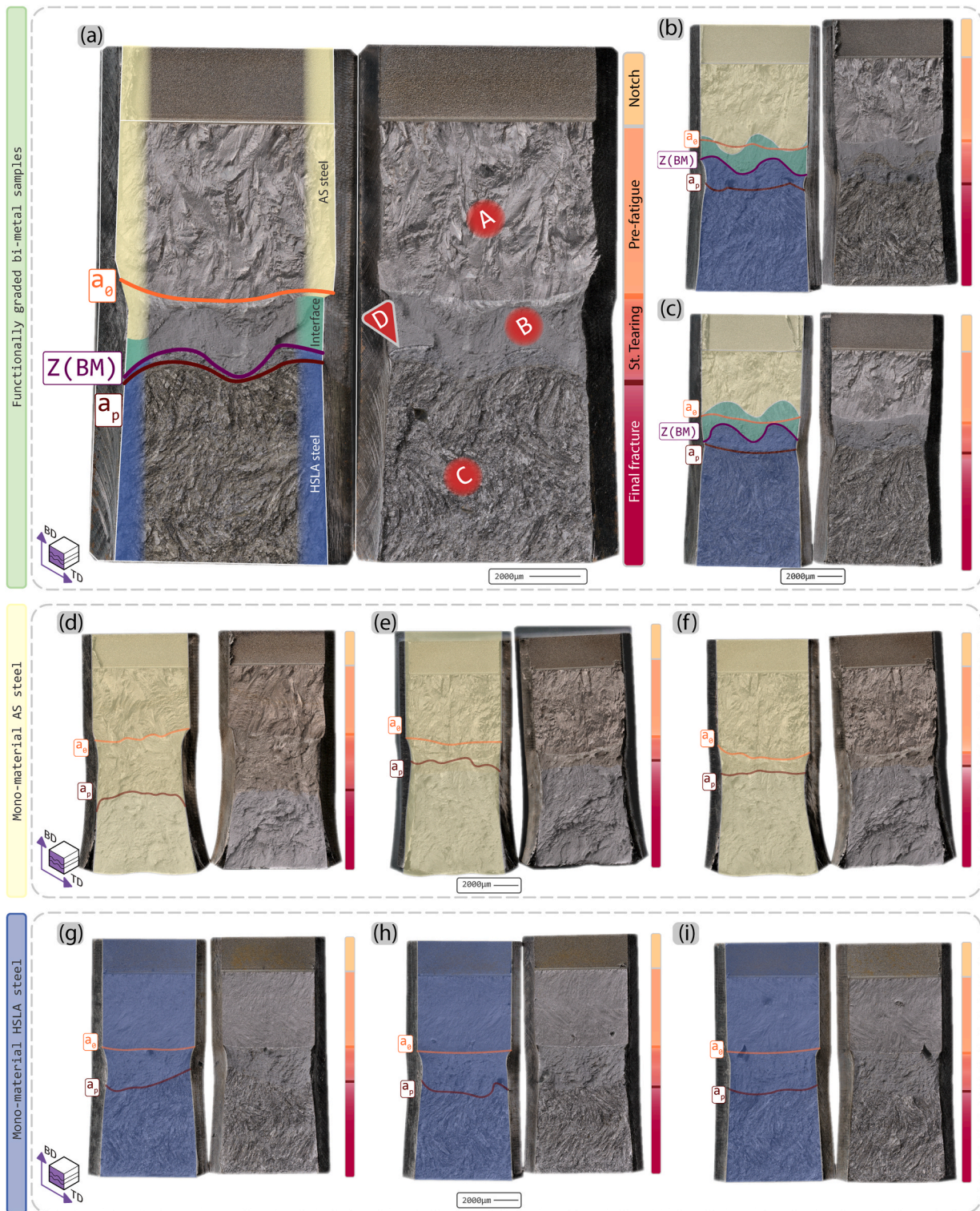


Fig. 6. Post-mortem macroscopic fractographic images of specimens (a) BM-A, (b) BM-B and (c) BM-D. (d–f) Fracture surfaces of AS steel specimens and (g–i) fracture surfaces of HSLA steel specimens. Features between two fracture surfaces of the same specimen appear mirrored.

smaller amount of material at the interface layer available to evaluate J_Q .

A particular challenge is derived from geometry of the dissimilar fusion line itself. Standard testing methods use a provision to ensure the validity of the linear-elastic solution for J_{el} . As mentioned in section 3.4, it is required for the crack front to stay straight and perpendicular to the faces of the specimen. This is enforced within a deviation of 0.1·

$(b_0 \cdot B_N)^{1/2}$ at any point along the average positions of a_0 and a_p lines. This value is about 950 μm given the pre-fatigue crack length and the specimen dimensions used in this study. All bi-material specimens comply with this provision when applied to the geometry of the interface layer. However, as the crack approaches the bi-material fusion line, local crack acceleration originating from the change in elastic domain is expected, in turn compromising the crack front straightness. The

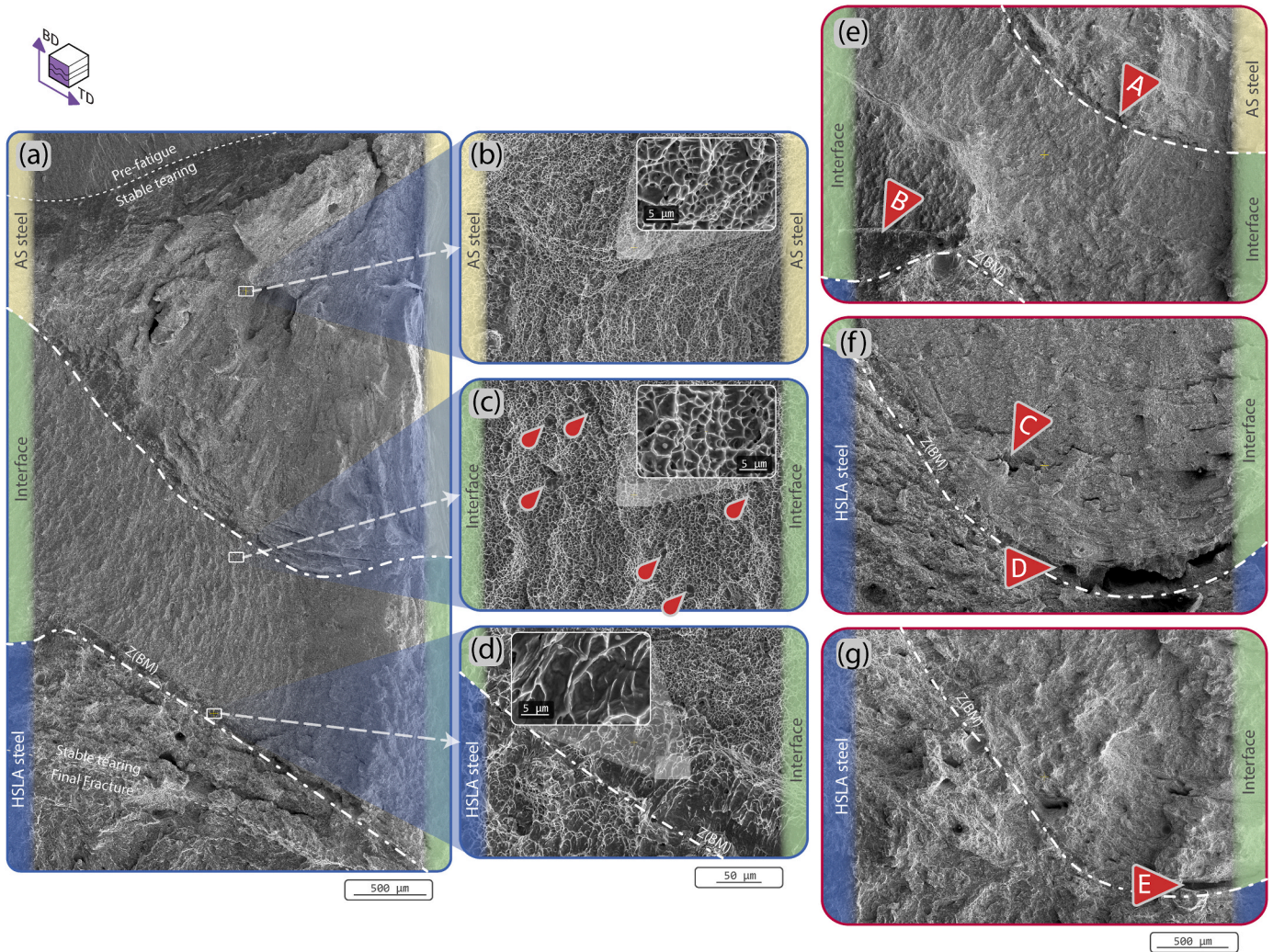


Fig. 7. Features observed under microscopic fractographic inspection of bi-material specimens. Micrographs include the (a–d) typical fracture features encountered along the stable tear region of a bi-material specimen in the (b) AS steel, (c) diluted interface material volumes and (d) the vicinity of the dissimilar fusion line. Micrographs (e–g) display examples of features encountered sporadically on different bi-material specimens, such as (e) signs of brittle fracture at the fusion boundary between the diluted interface layer and the undiluted AS steel (f) secondary crack formation perpendicular to the primary crack plane and (g) heterogeneous deformation along the dissimilar fusion line.

method implemented is considered sufficient to discern between the three material domains along a bi-material fusion line, although an accurate estimation on the position of the crack front, and with it, a direct correlation of defects found is challenging.

A closer look at the data used for regression is carried out to compare the differences in fracture behaviour of each material domain. To process the R-curve data shown on Fig. 5, the $J - \Delta a$ data pairs are used to fit an exponential function. It is from this fitted function that values J_Q and Δa_q are later derived. This entails that it possible to compare increments in J per increments in a in log-log space at different test stages. The data is plotted as such on Fig. 11 for the mono material specimens of (a) AS steel and (c) HSLA steel. The data plotted in (b) for the bi-material specimens is limited to those crack extension steps measured within the bi-material interface. On one hand it is made visible on the plots that both the AS steel and the HSLA mono-material data fall neatly together, displaying comparatively low dispersion. This can be correlated to the homogeneity on crack propagation process across the different layers of the additively manufactured material. The diluted interface layer in the bi-material specimens, on the other hand, is more disperse. This speaks to the degree of variability in local fracture toughness. Although data clusters mostly at lower values of $\log(a_{i+1}/a_i)$, a standard deviation an order of magnitude higher than that of the mono-material specimens is

obtained from the diluted interface layer. The fracture performance of the interface is thus the effect of a highly heterogeneous microstructure interacting with itself.

4.2. Shear banding, twinning, and metastable austenite transformation

The main strengthening mechanism at play across this bi-material part is revealed by the crack flanks of the cracked SENB specimens. It is observed that plastic strain is accommodated through shear banding, both on the undiluted AS steel and the diluted interface material volumes. For AS steels, specifically for 316L, this falls well in line with the available literature. Twinning gives way to the exceptional work hardening providing this excellent mechanical performance [29,51,52]. However, this observation entails a non-trivial process along the diluted interface layer due to its heterogeneous chemistry. Instead of twinning, martensite is observed at the crack flanks. This does not relate clearly to the fracture deformation mechanisms typically observed across acicular ferrite [50], but better resemble the observations made on the deformation mechanisms controlling plasticity in metastable austenite [53]. Thus, a deeper discussion on the underlying mechanisms of shear banding is necessary.

Since stacking fault energy (SFE) has been extensively correlated to

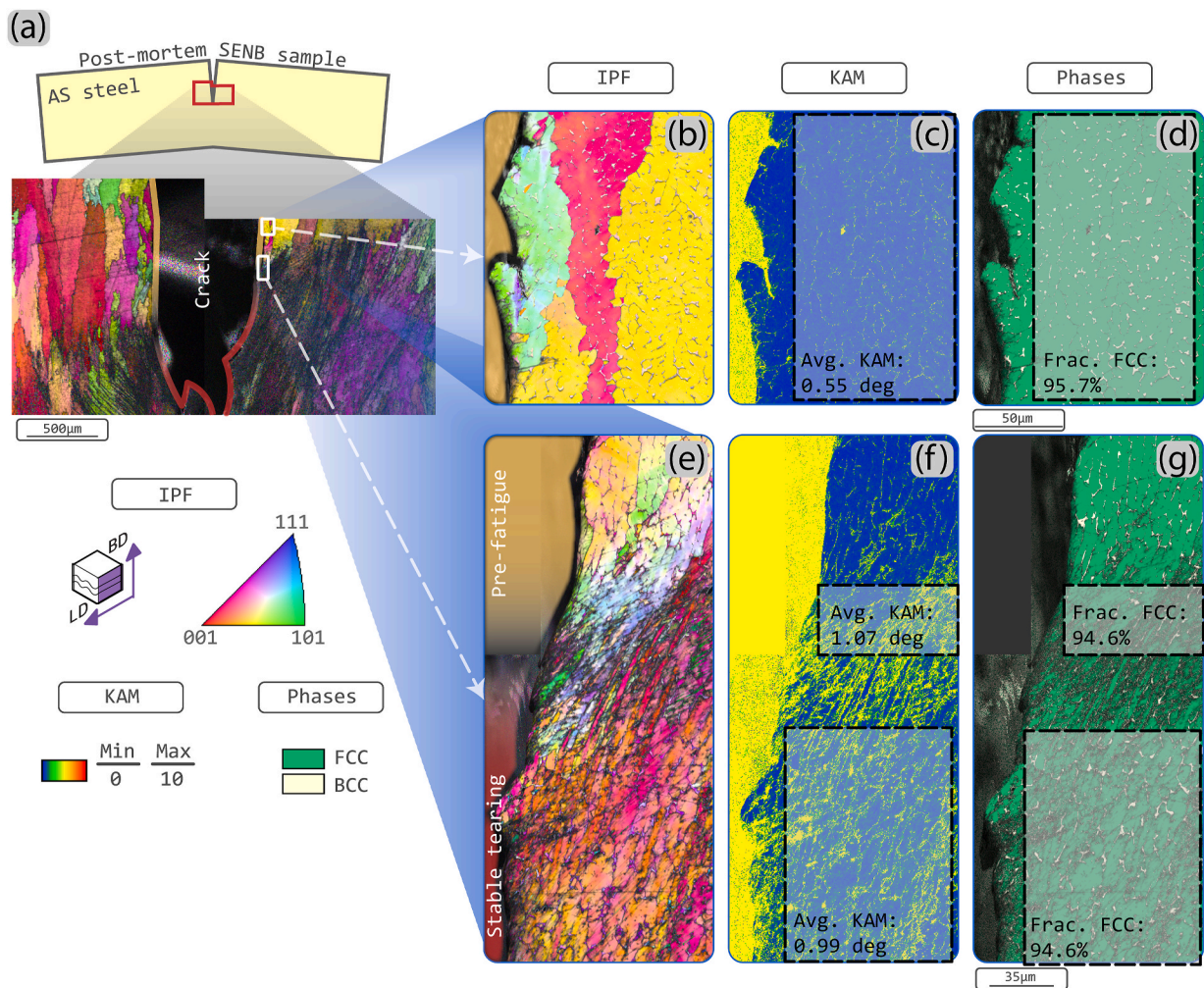


Fig. 8. EBSD map of crack flanks on an AS steel specimen. (a) IPF map stitched at a low resolution and 5 μm step size showing both crack flanks about a_0 . (b–d) IPF, KAM and phase maps of a crack flank in the region of pre-fatigue mapped with a step size of 0.1 μm. (e–g) IPF, KAM and phase maps stitched along the crack flank at a_0 , mapped with a step size of 0.1 μm. For IPF maps, $\langle 001 \rangle \parallel \text{BD}$.

the occurrence of either mechanical twinning or transformation-induced plasticity of metastable austenite, it is discussed in the context of this work. The SFE of different regions along the bi-material build as well as the nominal composition of the ER316L wire are presented in Table 5. The values for chemical composition are obtained from a previous related study [9], as measured through electron probe microanalysis. A distinction is made between the bulk of the diluted interface layer and the martensite bands running along it. This is done due to their distinct level of dilution. Martensite start temperature is included as a metric to emphasize this difference. Empirical models have been developed to estimate the SFE based on chemical composition. Although this method of estimating SFE is limited by the constrained nature of the data modelled [54], it serves as useful approximate indication. Thus, the random-intercept model presented by Meric de Bellefon et al. [55] is used, as it integrates data from many of the frequently cited models available in literature. The lower SFE values derived from the diluted chemistry of the interface support the notion that much of the martensite observed at the crack flanks originated from a TRIP effect.

EBSD mapping provides a useful path to map the extent of TWIN and TRIP effects on the deformed specimens through grain boundary analysis. In order to identify the TWIN effect, a practical approach is to map the $\Sigma 3$ boundary which most commonly follows a $\langle 111 \rangle / 60^\circ$ axis-angle relationship [51,57,58]. Alternatively, the TRIP effect can be highlighted through the martensite-austenite orientation relationship (OR). A Nishiyama-Wasserman (N-W) OR measured within a tolerance angle

of 5° will include most Kurdjumov-Sachs (K-S) and Greninger-Troiano OR's [59,60] obtained from this transformation. To do this, the axis-angle values of N-W OR used for EBSD mapping are $\langle 0.98 \ 0.08 \ 0.20 \rangle / 45.98^\circ$ [61,62]. To distinguish martensite from ferrite, an additional relationship is necessary. Helpful OR's have been established between the packages within martensite laths. Martensite packages in Mn-alloyed TWIP steels were observed to follow either K-S or N-W OR's. Morito et al. [63] identified an axis-angle of $\langle 101 \rangle / 60^\circ$ for martensite packages with a common $\langle 111 \rangle$ planes, although K-S OR foresees additional variants. Measurements by Suikkanen et al. [64] in Mn-Si-Cr steel show a preferential misorientation angle of $\langle 343 \rangle / 59.8^\circ$ between martensite laths. This indicates that mapping axis-angle relationships at 60° can help to distinguish contiguous martensite packages.

It is possible to correlate the SFE values with the OR discussed and examine the spatial distribution of these boundaries across the regions of interest. Given a value SFE of 27 mJ/m^2 , the AS steel mono-material specimen is expected to show extensive signs of twinning [57,65,66]. Taylor factors and axis-angle misorientations are mapped on Figs. 12 and 13. These maps are complimented with the calculated Taylor factor, as crystal orientation plays an important role on its capacity to accommodate strain by twinning [67,68]. Fig. 12 (b) shows disagreement between preferable crystal orientations and the mapped $\Sigma 3$ boundaries. Grains oriented closest to $\langle 111 \rangle \parallel \text{LD}$ show banding as obtained by the overlaid IQ values. Some of these bands are indicated by grey markers. Taylor factors are thus highest on what is suspected to be densely

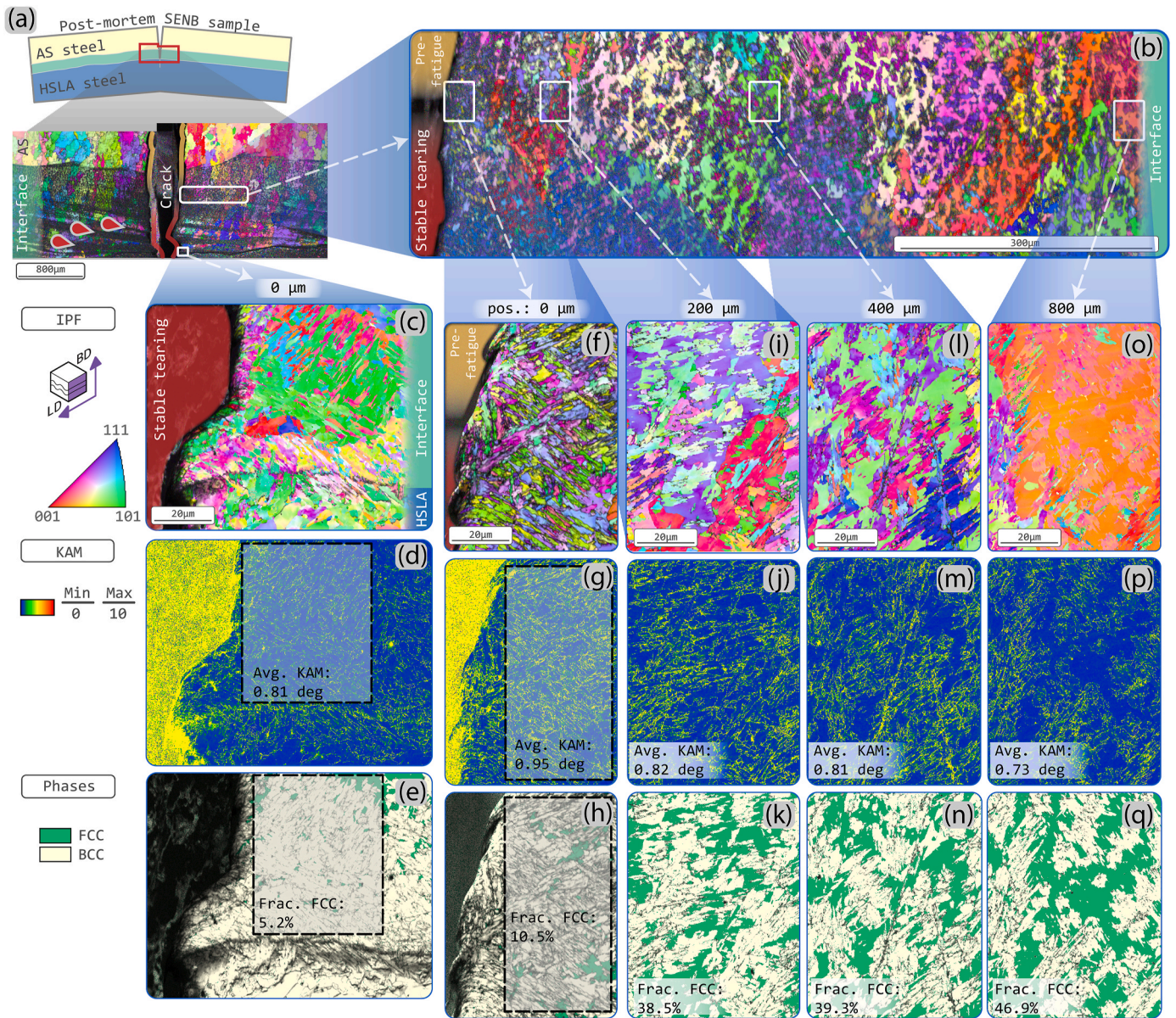


Fig. 9. EBSD mapping of crack flanks of a bi-material specimen. (a) IPF map stitched at a low resolution and 5 μm step size showing both crack flanks at a_0 . (b) A low magnification map of the region next to the a_0 point. (c–e) IPF, KAM and phase maps of the crack flank region in vicinity of the dissimilar fusion boundary. Detailed maps found within (b) alongside a_0 at the crack flank (f–h), as well as 100 μm (i–k), 400 μm (l–n), and 800 μm (o–q) away from the flank. For all IPF maps, $\langle 001 \rangle \parallel \text{BD}$.

twinned grains. The necessary resolution to map these boundaries accurately is not sufficient under the EBSD setting chosen, and it seems to be a frequently face problem for mechanically-induced twins [68,69]. Nonetheless, a very high value of the misorientation distribution function (MDF) for the $\langle 111 \rangle / 60^\circ$ between FCC phases shows a high occurrence of this OR, as shown on Fig. 13 (c). The MDF values around $\langle 111 \rangle / 60^\circ$ between BCC phases and $\langle 001 \rangle / 45^\circ$ between FCC-BCC phases matches the apparent lack of martensite in the mapped region.

The shear banding nature of the diluted interface layer is now discussed. With an estimated value SFE of 16 27 mJ/m², transformation to martensite by plastic deformation is expected. To obtain a quantitative measure of the TRIP effect across the heterogeneous diluted interface, three metrics are used. Firstly, the fraction of FCC on the maps increases as a function of position away from the crack flank, from 13.7 % in Fig. 9 (g) to 42.7 % in Fig. 9 (q). Due to lattice similarities, the body-centered tetragonal (BCT) crystal structure of martensite is often mapped as BCC. The phase fraction measured is thus convoluted by the fraction of ferrite

originating from solidification. As it was observed previously in a related study [9] under un-deformed conditions a BCC phase fraction of 40 % is expected for this specific part, although this number is subject to local heterogeneities.

Secondly, the effect of TRIP-assisted deformation is quantified by grain boundary analysis. Unlike the elusive twin boundaries in the undiluted AS steel, Bain-like N-W OR is extensively observed. This condition is met across most FCC-BCC boundaries mapped on Fig. 9. It shows an agreement between the expected parent-child couples but makes it difficult to distinguish between strain-induced martensite and allotropic martensite, if any is present. Also, the high angle grain boundary fraction between mapped BCC phases decreases as a function of distance, as it is measured through the MDF value shown for $\langle 111 \rangle / 60^\circ$. This high angle relationship decreases as a function of distance from the crack flank, giving an indication of a similar trend of the amount of martensite packages adjacent to each other.

The trend observed on the misorientation distribution function

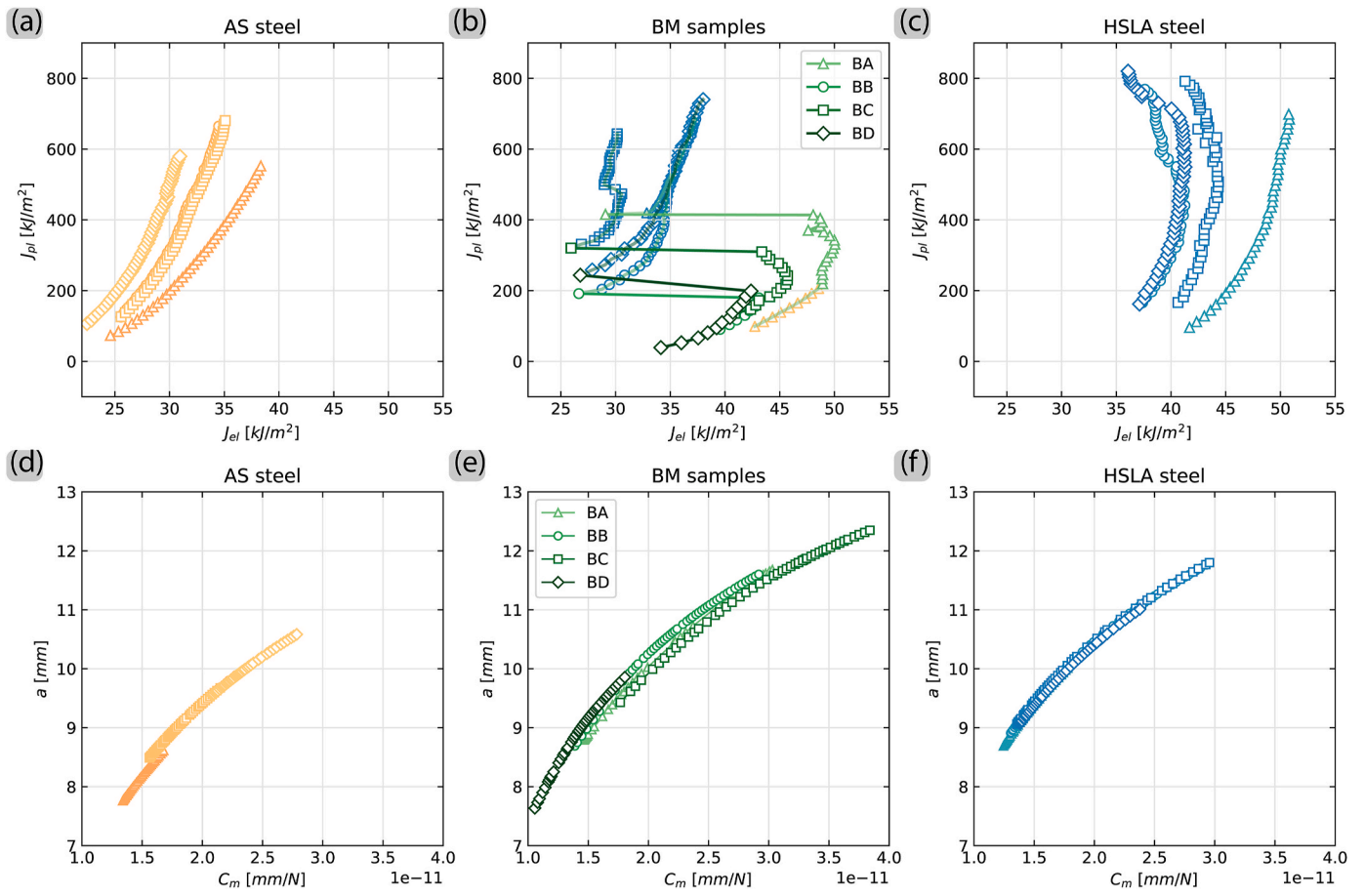


Fig. 10. Elastic vs. plastic components of J for (a) AS steel, (b) bi-material specimens and (c) HSLA steel and corresponding elastic compliance vs. crack length for each material condition (d-f).

(MDF) values of FCC phases about the $\langle 111 \rangle / 60^\circ$ misorientation requires further attention. As observed on TRIP-assisted steels [70,71], the strain hardening capacity is affected by both the interactions between harder and softer phases, as well as by the mechanical transformation of metastable austenite. Multiple studies noted that the austenite to martensite transformation rate would depend on the loading mode, the crystal orientation, and the grain size [72]. The larger, more favourably oriented austenite grains would then be expected to offer lower resistance to transformation than small grains less-favourably oriented. On one hand, the austenite crystal shown in Fig. 9 (c) displays a high Taylor value and low FCC-FCC $\langle 111 \rangle / 60^\circ$ value on the MDF. Interestingly, the crystal in Fig. 9 (c) shows similar IQ banding as the one observed in Fig. 9 (b). Fig. 9 (b-d, e) shows on the other hand lower Taylor values and higher MDF values for the same axis-angle relationship. These boundaries could then signify the effect of strain mismatch between a hard and a soft phase [72]. This needs to be confirmed nevertheless in a more detailed study.

Thirdly, a useful quantitative measure to characterize the TRIP effect is through KAM values. Opposite to the FCC phase fraction, KAM values decrease as a function of distance away from the crack flank. This is shown on Fig. 9 (g-p). It is helpful to note the findings by Shamsujjoha [73], where it is shown that KAM values of martensite do not tend to increase after deformation. Nevertheless, as noted by Jacques et al. [70], in order to accommodate the transformation of austenite into de martensite phase, dislocations pile up in the surrounding phases. Depending on the extent, this effect can be measured by KAM values. This reasoning also helps explain the low average KAM value obtained in Fig. 9 (d) and the high value observed in Fig. 9 (g). It matches the observation by Due et al. [74] in dual-phase and TRIP-assisted steels,

where it was concluded that lath martensite accommodates plastic deformation by boundary slipping. The authors also observed that the slippage of martensite packages caused strain in softer surrounding phase. Given the lack of work-hardening capacity of martensite, and its effect as a strain concentrator, it is necessary to discuss its effects on the crack propagation process.

4.3. Fracture after TRIP, allotropic martensite, and type II boundaries

Distinguishing itself from the bulk of the diluted interface layer, allotropic martensite is observed to promote brittle fracture. The location of cleavage features shown in Fig. 7 (c-g) matches that of the martensite typically found along the dissimilar fusion line, $Z(BM)$. The difference in fracture morphology between these two locations is attributed to the martensite fraction at each location. In both cases, the material cannot deform like its surroundings. As it is shown in Fig. 9, allotropic martensite retains only a very small amount of austenite. In the absence of austenite, two contiguous lath packages have no apparent work-hardening mechanism [70]. The mechanisms for plastic deformation are thus limited to the morphology of the laths, their dislocation density and their content of interstitials [72]. Controlling carbon content, tempering, or designing a heat treatment process that allows for a higher content of austenite could help overcome this problem. Tempered martensitic stainless steel, for example, yields a J_Q value of about $265 \pm 17 \text{ kJ/m}^2$ for compact tensile specimens with a retain austenite volume fraction of 15 % [75].

The effect of type II boundaries as a brittle feature is now brought into discussion. A type II boundary is understood to be caused by the migration of an austenite-austenite grain boundary across the fusion line

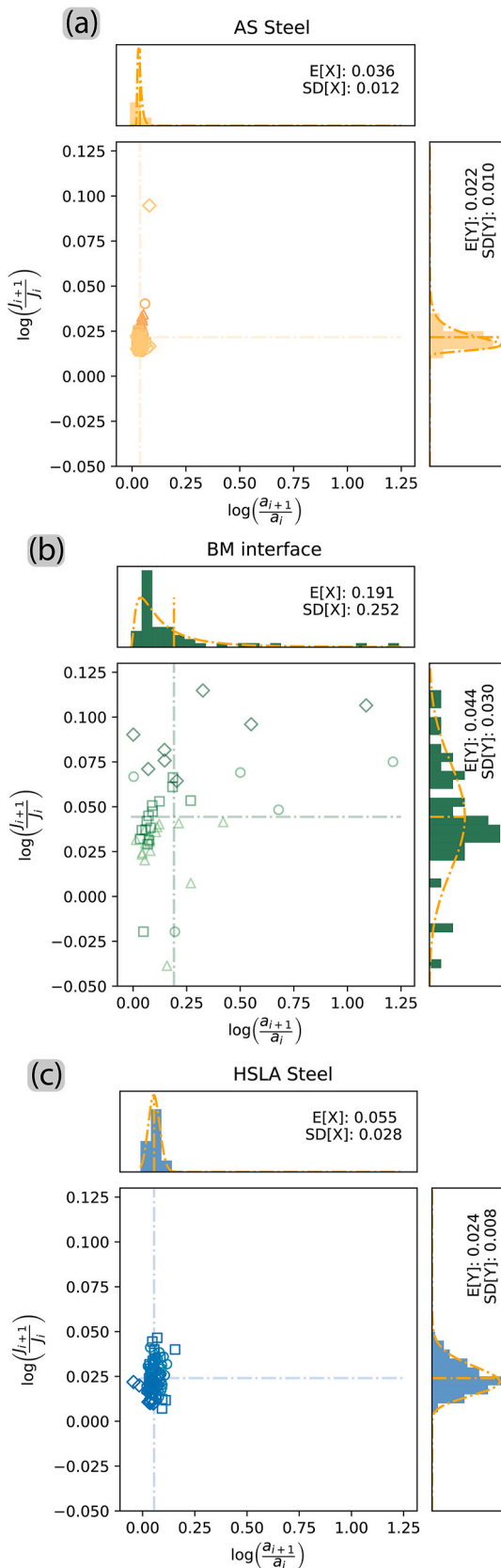


Fig. 11. Δ In log (a) vs. Δ in log (J) for (a) AS steel (b) bi-material specimens, constrained within the diluted interface layer, and (c) HSLA steel. Means ($E[X]$) and standard deviations ($SD[X]$) used to fit the scattered data to log-norm distributions are provided along each axis.

at very high temperatures, and successive heterogeneous allotropic transformations during cooling [23]. While characterizing the toughness of different regions around a dissimilar metal weld, Kumar et al. [76] demonstrated that the fusion line between Inconel and low-alloy steel produces type-II boundaries, and that this region exerts the least resistance to fracture. Ming et al. [77] show a similar result obtained through bending tests of dissimilar welds between a low-alloy steel and a Fe-Ni alloy. Type II boundaries may promote crack formation at lower strain levels than that of the surrounding matrix, although this effect may not be directly observed under monotonic tensile loading along the fusion line [78]. Ming et al. [77] also show that this type of boundary can promote intergranular fracture modes, similar to the ones found on the secondary crack highlighted in Fig. 7 (b).

Type II boundaries are detrimental defects found along the dissimilar fusion line of the bi-material block presented in this work. As shown in our previous study [9], the fusion line between the chosen AS and the HSLA steels show this feature occasionally. This type of boundary was found typically at the root of the welding tracks in the diluted interface layer. It matches the location shown on Fig. 7 (b), where a large secondary crack was formed. The fracture surface within this crack shows large extents of cleavage fracture accompanied by a few dimples oriented towards the BD direction. These features are shown in detail on Fig. 14 (c). The geometry of the crack and the orientation of the few dimples found suggest that this feature did not fail due to strain perpendicular to the plain of the main crack. In turn, these features suggest failure by strain parallel to the crack plane. This strain develops as the crack front approached, but had not yet reached, the dissimilar fusion line. This observation is supported by the magnitude of strain $\epsilon_{22} \parallel BD$, which is shown to be of comparable magnitude to the strain $\epsilon_{11} \parallel LD$, the leading strain component resulting in mode I loading. This is shown in Fig. 14 (b) as obtained from the FEM models detailed in Annex B.

5. Conclusions

Wire arc additive manufacturing provides a unique solution to manufacture compositionally graded parts of large dimensions. This compositional grading can be exploited to manufacture optimized parts in load bearing applications. Thus, it is necessary to understand the deformation and fracture behaviour of these heterogeneous parts. Through the extent of this work, the deformation and fracture toughness behaviour of wire arc additively manufactured ER70S-6-ER316L bi-material specimens was studied. As reported previously in our publication [9], the interface created by incomplete mixing of both alloys in a single weld pool shows a heterogeneous chemistry, and with it, a highly heterogeneous microstructure. Digital image correlation was used in the current study to investigate the local strain behaviour of this bi-material interface region during quasi-static tensile loading. Based on the results obtained from DIC measurements, FEM analysis was used to provide correction functions for a J-integral solution specific for bi-material specimens. Fracture toughness values were obtained to measure the layer's resistance to crack extension and scanning electron microscopy with electron back-scatter diffraction were used to inspect the deformation around the crack flanks and at the fracture surface. From this work, the following conclusions are drawn.

- The elastic modulus of the diluted bi-material interface is shown to closely match that of the un-diluted AS steel at a value of 157 ± 17 GPa. Digital image correlation exposed also macroscopic shear banding and a variable strain-hardening development in at this interface region.
- The sharp change in elastic modulus of a bi-material specimen entails also a discontinuity in the J-integral formulation.
- Fracture toughness of the interface is shown to yield a J_{IC} value of 180 kJ/m^2 . The value is lower than that measured of mono-material AS steel specimens (458 kJ/m^2) and HSLA steel (408.1 kJ/m^2). The

Table 5

Chemical composition in wt%, martensite start temperature (M_s) and room temperature stacking fault energy (SFE) for regions of interest across the bi-material part, and the nominal composition of the AS wire consumable. Data provided ± 1 standard deviation.

	[C]	[Si]	[Cr]	[Mn]	[Mo]	[Ni]	Other	M_s^a °C	SFE ^b mJ/ m ²
Diluted interface layer, excluding martensite bands	0.02 ± 0.01	0.56 ± 0.05	14.49 ± 0.88	1.63 ± 0.16	2.11 ± 0.23	8.65 ± 1.09	–	-84 ± 60	20 ± 2
Martensite band within diluted interface layer	0.03 ± 0.02	0.7 ± 0.06	10.48 ± 1.52	1.64 ± 0.08	1.5 ± 0.23	6.54 ± 0.93	–	83 ± 62	16 ± 2
AS steel layer 2	0.01 ± 0	0.41 ± 0.04	16.87 ± 0.78	1.52 ± 0.12	2.52 ± 0.26	8.97 ± 0.95	–	-153 ± 42	21 ± 2
ER316L Nom. Comp. ^c	0.02	0.45	18.50	1.60	2.60	12.00	[N]: 0.04	-326	27

^a $M_s = 526 - 354[C] - 29.7[Mn] - 31.7[Si] - 12.5[Cr] - 17.4[Ni] - 20.8[Mo]$ [56].

^b $SFE = 2.2 + 1.9[Ni] - 2.9[Si] + 0.77[Mo] + 0.5[Mn] + 40[C] - 0.016[Cr] - 3.6[N]$ [55].

^c [45].

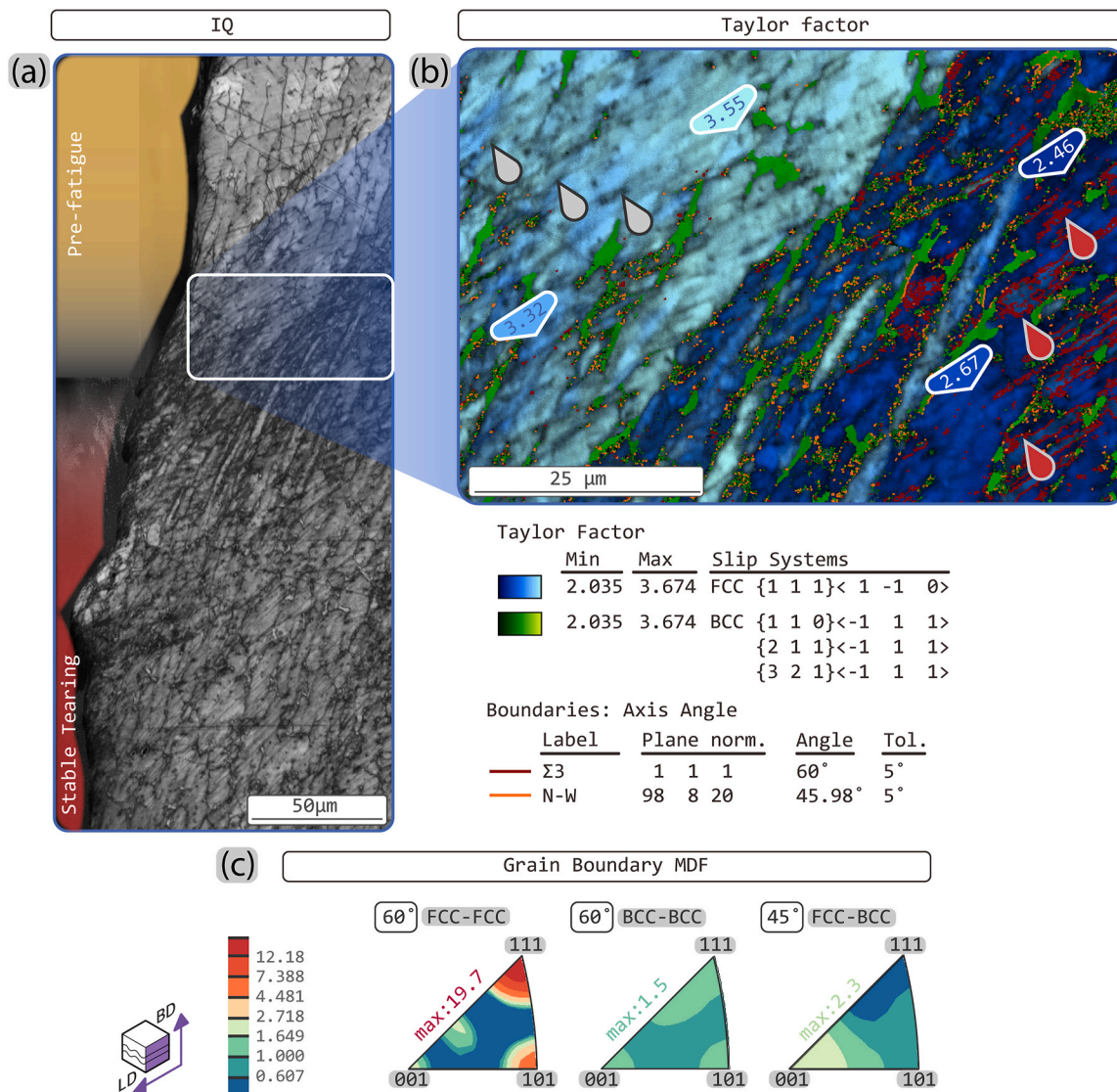


Fig. 12. (a) Low-magnification IQ map of AS steel crack flank about a_0 . The location matches that on Fig. 8 (e). (b) Taylor factor map (blue colour scale indicates FCC phase, green colour scale indicates BCC phases) annotated with the specific values calculated at representative locations. Colour scales and slip systems are included in the legend. IQ mapping is overlaid as grey scale. Grain boundaries indicating $\Sigma 3$ OR suggesting twinning and N-W OR for $\gamma \rightarrow \alpha$ transformation are shown in color. (c) Grain boundary ODF shown for axis/angle relationships of interest, within a misorientation tolerance of 5° .

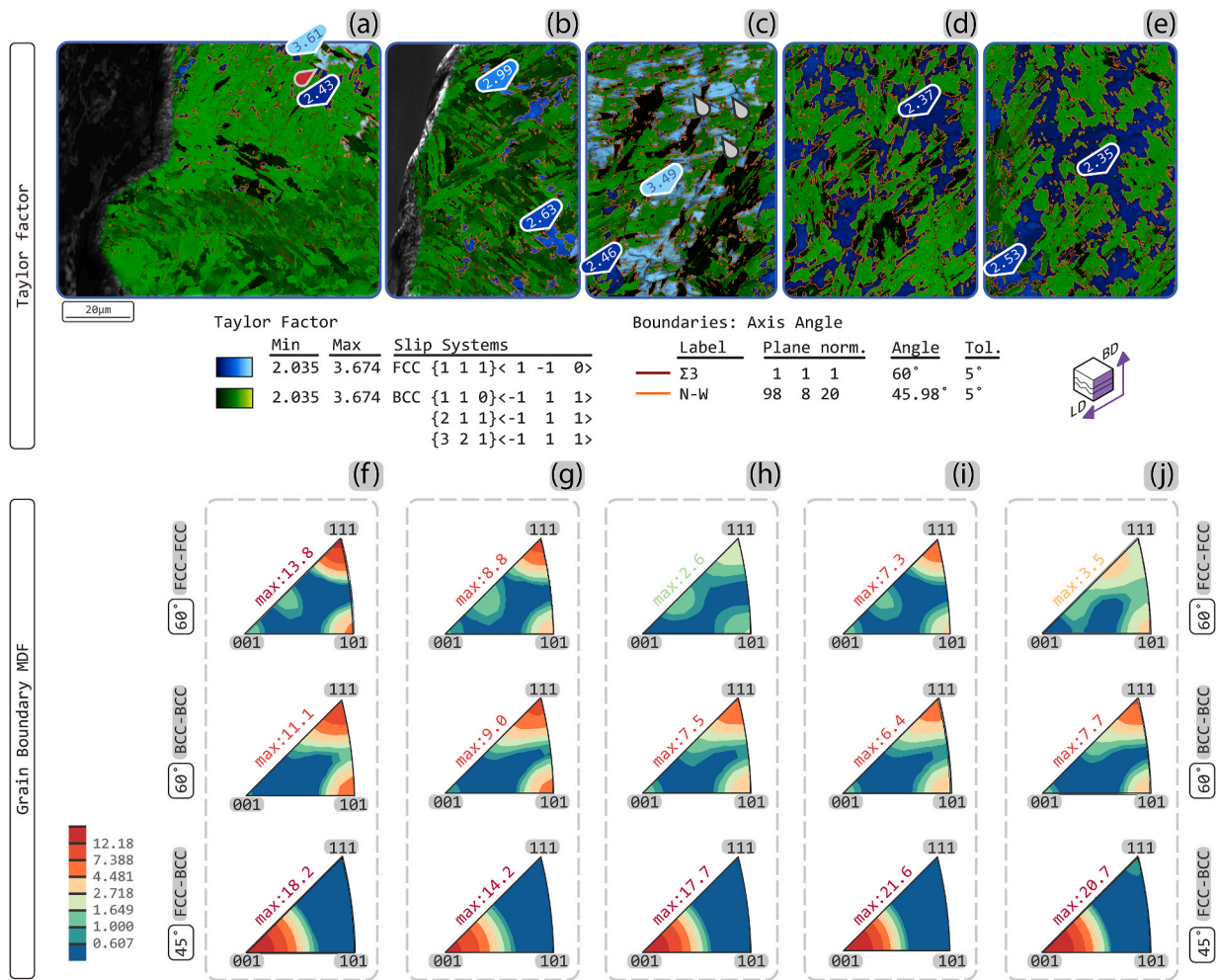


Fig. 13. (a–e) Taylor factor maps of areas shown on Fig. 9 (c, f, i, l o). Blue color scale indicates FCC phase, green colour scale indicates BCC phases. Maps are annotated with the specific values calculated at representative locations. Color scales and slip systems are included in the legend. IQ maps are overlaid as greyscale. Grain boundaries indicating $\Sigma 3$ OR for twinning and N-W OR for $\gamma \rightarrow \alpha$ transformation are shown in color. (f–j) Grain boundary ODF shown for axis/angle relationships of interest, within a misorientation tolerance of 5° for each corresponding area mapped on figures (a–e).

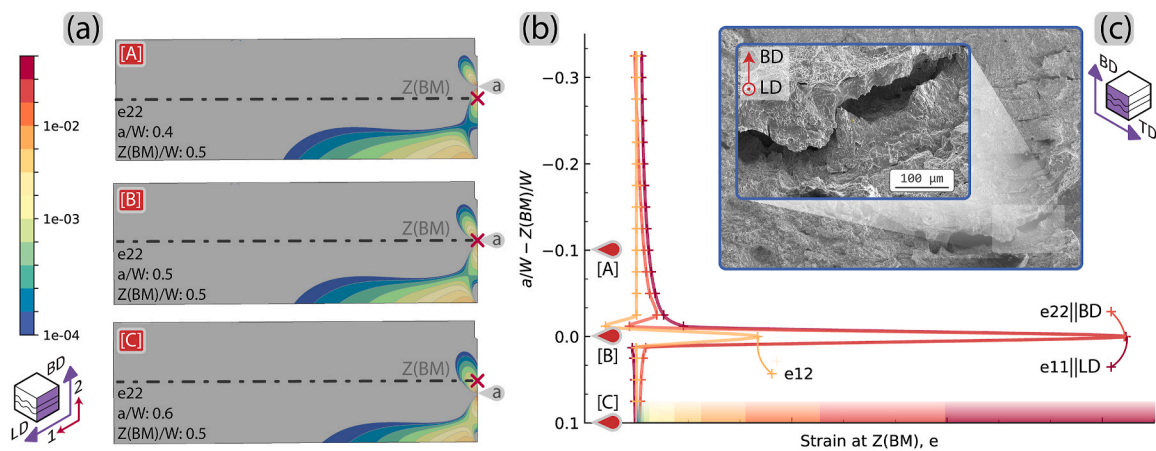


Fig. 14. FEM results mapping e_{22} strain for values $a/W - Z(BM)/W$ equal to $-0.1, 0.0$ and $+0.1$. (b) Principal strain components e_{11} and e_{22} , as well as shear strain e_{12} as measured at the intersection between the crack plane and $Z(BM)$. Values plotted as a function of $a/W - Z(BM)/W$, to understand the effect of an approaching crack on the measured local strain. (c) Fracture surface at the location where a type II boundary is expected.

value obtained from the interface value is nevertheless comparable with other TRIP steels and tempered martensitic stainless steels.

- The fracture surface of the interface shows mostly ductile behaviour, with features of quasi-cleavage fracture. It should be noted that type II boundaries and martensite are observed to cause large amounts of dispersion in the measured toughness values of the interface layer.
- Post-mortem inspection through EBSD mapping of the crack flanks confirms a change in governing deformation mechanism from twinning induced plasticity to transformation induced plasticity, as suggested by the DIC results. This is attributed to the diluted chemistry obtained during deposition.

Through the extent of this work, the effect of chemical dilution on the deformation mechanisms and fracture toughness of bi-material component was evaluated. The correlative use of microscopic, mechanical and FEM analysis proved necessary to understand the underlying fracture micro-mechanisms governing the behaviour of such complex interface layer. The results indicate that the interface develops a lower resistance to fracture if compared to the un-mixed alloys, which needs to be accounted for in the design of parts composed by this bi-metal couple. Subsequent layers of AS steel cladding show adequate monotonic and fracture behaviour, demonstrating that multi-layer cladding would be advisable for structural applications. The work thus provides empirical evidence on the effects of manufacturing compositionally graded steel structures through WAAM and establishes a baseline for further process design and optimization.

Annex A. True stress, true strain, and work-hardening relationships obtained from DIC

True strain is obtained based on the Hollomon relationship [79], given that:

$$\varepsilon = \ln(1 + e) \quad (\text{Eq. A1})$$

where e is the engineering strain as measured by the digital DIC strain gauges, s is the engineering stress, σ is the true stress and ε the true strain. Similarly, the true stress values are derived from the digital strain gauge measurements as follows:

$$\sigma = s \cdot (1 + e). \quad (\text{Eq. A2})$$

Since necking occurs away from the region measured, this relationship stays true through all measured points. Having obtained the true strain-stress relationships, it is possible to obtain the work hardening rate (WHR), such that:

$$\Theta = \frac{d\sigma}{d\varepsilon}. \quad (\text{Eq. A3})$$

For the data given, $d\sigma$ and $d\varepsilon$ are computed based on the numerical differences of two subsequent data points. The values obtained are plotted in Fig. 3 (c) and (d) for the two set of tensile specimens measured. Due to the noise derived from the numerical operation to obtain the WHR, a moving average regression of order 5 is provided with an error band equivalent to ± 1 standard deviations. In the case of bi-metal specimens, the moving average regression is applied only on values where $\varepsilon > 3\%$ to emphasize the work-hardening behaviour caused by the TRIP effect.

Annex B. LE-FEM analysis in detail

The intention of this annex is to elaborate on the finite element model used to obtain $J_{eL,FEM,BM}$ and $C(a/W)_{FEM,BM}$ mentioned in Section 2.3.1 (Eq. (1)) and (Eq. (3)).

The dimensions and boundary conditions of the modelled specimen were representative to those of the physical specimens tested. Exploiting the symmetry around the crack plane, a model was defined in ABAQUS consisting of half an SENB specimen. The material properties chosen are isotropic and linear elastic. As it is demonstrated in section 3.1, the diluted interface layer and the AS steel show an elastic modulus of 160 GPa, whereas the HSLA steel shows an elastic modulus closer to 210 GPa. The FEM models were thus fully described by two regions with different elastic moduli. Models were built for values of a/W and $Z(BM)/W$ ranging between 0.175 and 0.850, at increments of 0.0125 in both cases. The model features a width W of 10 mm and a support span S equal to $4 \bullet W$. A prescribed displacement (δ) of 0.1 mm parallel to the negative BD was set on an edge segment of 0.2 mm length at a distance $S/2$ away from the crack plane. To counter the prescribed displacement, a 0.1 mm support was modelled fixed with a 0 mm displacement directly ahead of the crack front. The mesh topology, boundary conditions and elastic property assignment are shown in Fig. B-1 (a). Fig. B-1 (b) shows the location of half the CMOD measurement at the crack mouth by superimposing the deformed and undeformed modelling results. To give an indication of the strain values obtained through this numerical analysis, the strain component $e_{11} \parallel LD$ is mapped on the latter figure.

Adequate meshing and section definitions are necessary to obtain reliable J -integral values. Quadrilateral eight-node plane strain elements with full integration were used. Symmetry boundary conditions are set along the ligament up to the crack front to reduce the number of elements. The elements around the crack tip consist of collapsed quadrilateral elements with single nodes around the tip vertex, as shown on Fig. B-1(c). Strain

CRediT authorship contribution statement

J.L. Galán Argumedo: Writing – review & editing, Writing – original draft, Visualization, Methodology, Investigation, Formal analysis, Data curation, Conceptualization. **A.C. Riemslog:** Writing – original draft, Investigation, Formal analysis. **M.J.M. Hermans:** Writing – review & editing, Supervision, Resources, Project administration, Funding acquisition, Conceptualization. **V.A. Popovich:** Writing – review & editing, Supervision, Resources, Project administration, Funding acquisition, Conceptualization.

Declaration of competing interest

The authors declare the following financial interests/personal relationships which may be considered as potential competing interests: Marcel Hermans reports financial support was provided by European Commission.

Acknowledgements

This research is supported by the Materials innovation institute M2i (www.m2i.nl).

This project has been financed by the program of Research and innovation Horizon2020 of the European Union under the Grant Agreement No. 862017.

singularity around the crack tip is controlled as a function of $1/\sqrt{r}$ by moving the mid-side nodes to the 1/4 points. The J -integral calculation relies on a series of concentric paths around the crack tip. For every geometry modelled, the J -integral is evaluated at the 10th concentric path, described by a radius approximately equal to $0.002 \cdot W$.

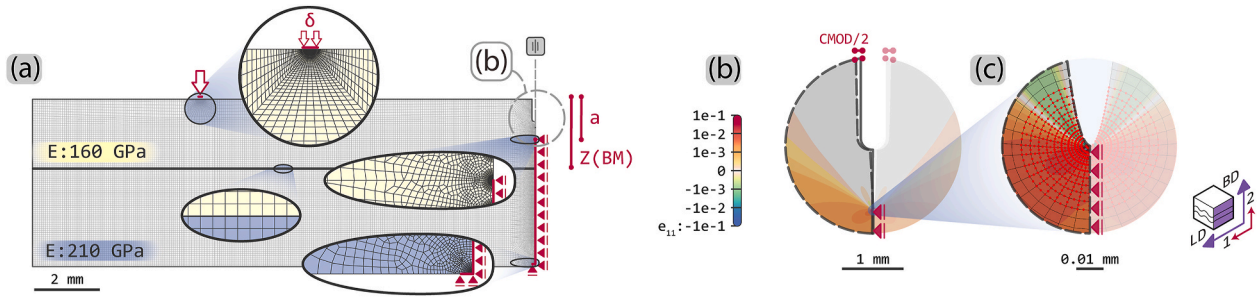


Fig. B-1. Finite element model showing (a) boundary conditions, material assignments and mesh topology, as well as the definition of the variables a and $Z(BM)$. (b) Measurement location for CMOD, on undeformed and deformed geometries. (c) Detail on mesh topology and J -integral integration nodes at the crack front on a deformed geometry. (b - c) show geometries 5x exaggerated with e_{11} strain values plotted for $a/W = 0.25$ and $Z(BM)/W = 0.6$.

As observed in section 3.1, the elastic response of the diluted interface layer shows small variability for the loading condition studied. Moreover, the elastic properties of the diluted interface layer fairly resemble those of an un-diluted ER316L all-weld-metal deposit. As a result, and under these simplified conditions, both materials are expected to behave homogeneously under linear-elastic deformation. Consequently, the only interface considered is that between the diluted interface layer and the HSLA steel material volume. The elastic values obtained are taken as an input to study the effect of elastic heterogeneity across a bi-material interface.

The results obtained from the linear-elastic J -integral FEM calculations are provided on Fig. B-2. Fig. B-2 (a) shows the values obtained of J -integral as a function of the crack depth, a , and the position of the bi-material fusion line $Z(BM)$ as measured from the notched surface. The values of J -integral are plotted against the FEM results for a mono-material SENB specimen of identical dimensions of elastic moduli of 160 GPa and 210 GPa independently. Given that analytical solutions for the J -integral values exist for mono-material conditions, this $a - J$ relationship is also presented, given that [34]:

$$J_{I,el} = G_I = \frac{K_I^2 \cdot (1 - \nu^2)}{E} \quad (\text{Eq. B1})$$

for plain strain conditions, where G is the strain energy release rate, K is the stress intensity factor, ν is the Poisson's ratio and E is the elastic modulus. The index I is used to indicate mode I loading. Given the loading conditions at the quasi-static crack front region for a 3-point single edge notched bending specimen (SENB3), this is the only load mode considered. Thus, this index is not used further for brevity. The relationship between a and J is made explicit if it is considered that [34]:

$$K = \left[\frac{P \cdot S}{(B \cdot B_n)^{1/2} \cdot W^{3/2}} \right] f\left(\frac{a}{W}\right) \quad (\text{Eq. B2})$$

where P is the total load, S is the span between supports, B and B_n are the un-grooved and the grooved specimen thicknesses correspondingly, and W is the specimen's width. The function $f(a/W)$ is the geometry-dependent relation between the load applied and the stress intensity factor. For a standard SENB3 specimen, this function is formulated as [34]:

$$f\left(\frac{a}{W}\right) = \frac{3 \cdot \left(\frac{a}{W}\right)^{1/2} \cdot \left[1.99 - \left(\frac{a}{W}\right) \cdot \left(1 - \left(\frac{a}{W}\right)\right) \cdot \left(2.15 - 3.93 \cdot \left(\frac{a}{W}\right) + 2.7 \cdot \left(\frac{a}{W}\right)^2\right) \right]}{2 \cdot \left(1 + 2 \cdot \frac{a}{W}\right) \cdot \left(1 - \frac{a}{W}\right)^{3/2}} \quad (\text{Eq. B3})$$

The values of J -integral are thus demonstrated to vary between the boundaries of the mono-material solutions for the elastic moduli considered. This is true with exception of the J values obtained near the bi-material interface. When the depth of the crack front approaches $Z(BM)$, the values of J rapidly drop. This can be interpreted as less energy input being necessary to achieve an infinitesimal extension of the crack front as it approaches the bi-material boundary. Having crossed the bi-material boundary, the values rapidly increase. The J value then gradually approaches that of the mono-material condition of the underlying metal.

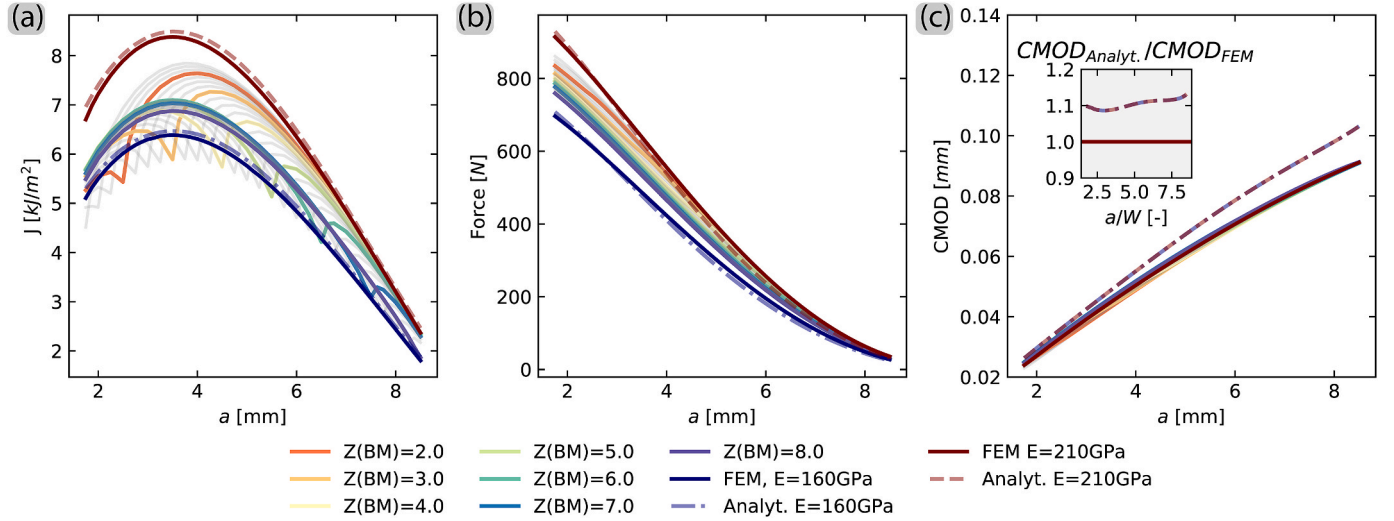


Fig. B-2. (a) J integral, (b) resultant force and (c) CMOD measurements obtained from linear-elastic composite SENB specimen under a 0.1 load-line displacement for different positions of the bi-material interface $Z(BM)$. Results are shown in colour for every 1 mm increment of $Z(BM)$, and in grey for every 0.25 mm increments. Analytical and FEM solutions for mono-material specimens are provided as a reference. Inset in (c) shows ratio between CMOD values for the analytical solution with respect to the FEM calculations.

The force compliance as a function of a and $Z(BM)$ is presented in Fig. B-2(b). Like the results presented for J -integral, the results for bi-material geometries are accompanied by FEM results of mono-material conditions for the 2 elastic moduli of interest, and two analytical solutions. In this case, the analytical solution is provided by Ref. [34]:

$$P = \frac{v_{LL}}{C_{LL}} \quad (\text{Eq. B4})$$

where v_{LL} is the load-line displacement and the force vs. load-line compliance, C_{LL} , is defined analytically as follows [34]:

$$C_{LL} = \frac{1}{E \cdot B_e} \left(\frac{S}{W-a} \right) \cdot \left[1.193 - 1.98 \cdot \left(\frac{a}{W} \right) + 4.478 \cdot \left(\frac{a}{W} \right)^2 - 4.443 \cdot \left(\frac{a}{W} \right)^3 + 1.739 \cdot \left(\frac{a}{W} \right)^4 \right] \quad (\text{Eq. B5})$$

where $B_e = B - (B - B_n)^2 / B$. The load can then be easily estimated, given that the modelling conditions impose a load-line displacement of 0.1 mm in all instances. For the FEM models, the load is simply obtained as the global reaction force. The compliant loads obtained from the bi-material specimen models neatly fall within the boundaries set by the mono-material models. However, the FEM solutions appear to overestimate the resulting load for crack depth values larger than 3 mm when they are compared to the analytical solutions.

The opposite problem is observed when analysing the results of CMOD vs. crack depth values. On this occasion, the FEM results underestimate the CMOD values when compared to the analytical solution. The latter is taken from the relationship between load and CMOD, such that:

$$v_m = CMOD = P \cdot C_m \quad (\text{Eq. B6})$$

where v_m is the crack-mouth opening displacement and C_m is the load-CMOD compliance relationship. The analytical solution for C_m is stated as follows [34]:

$$C_{m,analyt} = \frac{6 \cdot S}{E \cdot W \cdot B_e} \left(\frac{a}{W} \right) \cdot \left[0.76 - 2.28 \cdot \left(\frac{a}{W} \right) + 3.87 \cdot \left(\frac{a}{W} \right)^2 - 2.04 \cdot \left(\frac{a}{W} \right)^3 + \frac{0.66}{(1 - a/W)^2} \right] \quad (\text{Eq. B7})$$

The relationship of CMOD vs. a is identical for both elastic moduli of interest. This is true, given that to compute the analytical value of v_m , the corresponding mono-material P values were used as obtained from the FEM analyses. To overcome this difference between analytical and FEM formulations, an error function is obtained as a 4th order polynomial regression which is independent of the elastic modulus, namely:

$$e_m \left(\frac{a}{W} \right) = \frac{CMOD_{Analyt.}}{CMOD_{FEM}} = 0.0003 \cdot \left(\frac{a}{W} \right)^4 - 0.0061 \cdot \left(\frac{a}{W} \right)^3 + 0.048 \cdot \left(\frac{a}{W} \right)^2 - 0.1498 \cdot \left(\frac{a}{W} \right) + 1.2467. \quad (\text{Eq. B8})$$

This regression result is shown graphically in the inset of Fig. B-2 (c). The bi-material solutions obtained through FEM closely resemble the solution obtained from mono-material conditions. Nonetheless, for all values of $Z(BM)$ a similar trend is found: CMOD values are typically higher when $a < Z(BM)$, and lower when the opposite relationship is true. Also, the largest relative difference $CMOD_{BM}/CMOD_{MM}$ ranges between 1.05 and 0.99 for $Z(BM) = 6$ mm, under a non-linear relationship with a/W .

Annex C. Numerical evaluation of Γ_J^E and Γ_C^E

Fig. C-1 (a) and Fig. C-1 (b) show the ratio between the results obtained from FEM analysis of a bi-material specimen and the analytical expressions for J -integral available in the literature. This is done through the normalized error functions Γ_J^{160} and Γ_J^{210} defined on Eq. (1). Since $G_{Analyt.MM}^E$ is a function of the elastic modulus, a superscript 210 or 160 is used to denote the value of E used. Fig. C-1 (a) gives the ratio between the J_{el} and G values as

a function of crack tip and bi-material interface positions. The values are normalized by the analytical solution of G describing an isotropic specimen with an elastic modulus of 160 GPa. Fig. C-1 (b) shows the same relationship for a specimen with an elastic modulus of 210 GPa. The domain of Fig. C-1 (a) is constrained to values where $a/W < Z(BM)/W$. Similarly, Fig. C-1 (b) is constrained to a domain of $a/W > Z(BM)/W$. These two conditions are set considering the geometry and loading direction of the bi-material specimens tested in this work.

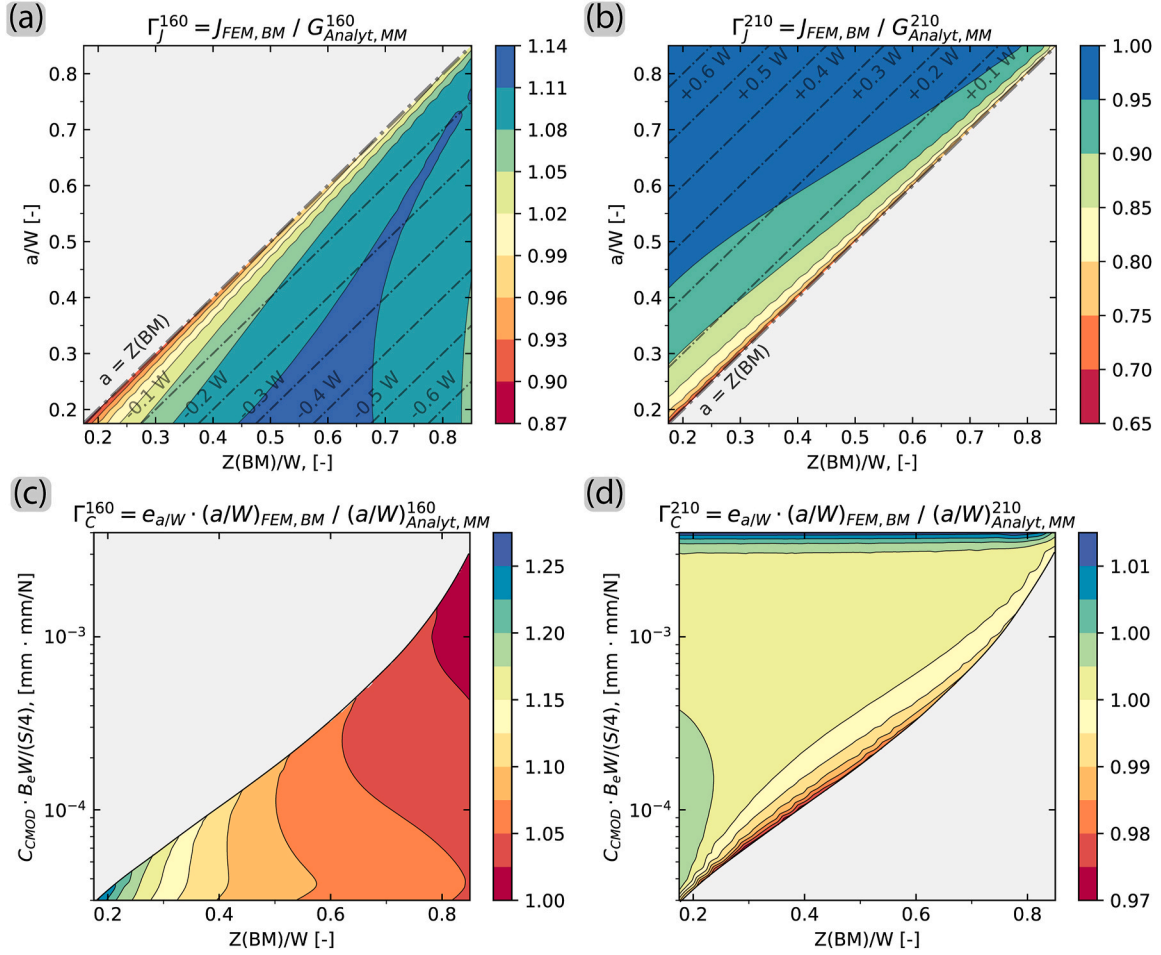


Fig. C-1. (a) J -integral values obtained from bi-material SENB FEM model normalized by G values of a mono-material specimen with $E = 160$ GPa as a function of crack position a/W , and position of bi-material interface $Z(BM)$ (b) J -integral values normalized by G with $E = 210$ GPa. Iso-distant curves of the crack front position with respect to the bi-material interface are provided each $0.1W$. (c-d) a/W as a function of CMOD compliance and bi-material interface position, normalized by the analytical solution for mono-material specimens.

Fracture toughness results are derived from the evaluation of the crack length as a function of CMOD compliance. Hence the need for such relationship to be established. Eq. (B5) provides a useful solution to obtain the compliance values as a function of relative crack depth. Nonetheless, during testing the inverse relationship between C_m and a is necessary. An analytical relationship is available in literature, such that [34]:

$$C(a/W)_{Analyt,MM} = [0.999748 - 3.9504 \cdot u + 2.9821 \cdot u^2 - 3.21408 \cdot u^3 + 51.51564 \cdot u^4 - 113.031 \cdot u^5] \quad (\text{Eq. C1})$$

where:

$$u = \frac{1}{\left[\frac{B_e \cdot W \cdot E \cdot C_m}{S/4} \right]^{1/2}} \quad (\text{Eq. C2})$$

In this case, C_m is the experimentally measured v_m/P compliance. As established on Eq. (B8), a correction factor is necessary to bridge the error between the FEM-modelled CMOD compliance and the one obtained from the analytical relationship. To obtain the correct relationship between Eq. (B5) and the predicted crack length values, the inverse function to Eq. (B8) is necessary, such that:

$$e_m^{-1} \left(\frac{a}{W} \right) = e_{a/W}(C_m). \quad (\text{Eq. C3})$$

This function is solved numerically through interpolation of the function e_m^{-1} for the known value pairs of $(C_m, a/W)$.

Having established the necessary relationship between C_m and a , an error function can be defined to relate the standard analytical relationships with the experimental data obtained from a bi-material specimen. The sought relationship establishes the connection between the predicted values of $(a/W)_{BM}$ and $(a/W)_{MM}$ as a function of compliance and position of the bi-material interface. The numerical solution is presented in Fig. C-1 (c) and (d), following the relationship established in Eq. (3). Fig. C-1 (c) shows the values to this function for the domain where $(a/W) = e_{a/W}(C_m) \cdot (a/W)_{FEM,BM} <$

$Z(BM)/W$ and Fig. C-1 (d) for the domain where $(a/W) = e_{a/W}(C_m) \cdot (a/W)_{FEM,BM} > Z(BM)/W$.

Data availability

Data will be made available on request.

References

- [1] R. Zhang, F. Jiang, L. Xue, J. Yu, Review of additive manufacturing techniques for large-scale metal functionally graded materials, *Crystals* 12 (6) (2022), <https://doi.org/10.3390/cryst12060858>.
- [2] L.P. Raut, R.V. Taiwade, Wire Arc additive manufacturing: a comprehensive review and research directions, *J. Mater. Eng. Perform.* 30 (7) (2021) 4768–4791, <https://doi.org/10.1007/s11665-021-05871-5>.
- [3] B. Wu, et al., A review of the wire arc additive manufacturing of metals: properties, defects and quality improvement, *J. Manuf. Process.* 35 (August) (2018) 127–139, <https://doi.org/10.1016/j.jmapro.2018.08.001>.
- [4] A. Babu, A. Ebrahimi, K.H. Wu, I.M. Richardson, M.J.M. Hermans, Local control of microstructure and mechanical properties of high-strength steel in electric arc-based additive manufacturing, *J. Mater. Res. Technol.* 26 (2023) 1508–1526, <https://doi.org/10.1016/j.jmrt.2023.07.262>.
- [5] J. Wang, et al., Characterization of wire arc additively manufactured titanium aluminide functionally graded material: microstructure, mechanical properties and oxidation behaviour, *Mater. Sci. Eng., A* 734 (July) (2018) 110–119, <https://doi.org/10.1016/j.msea.2018.07.097>.
- [6] T.A. Rodrigues, et al., Steel-copper functionally graded material produced by twin-wire and arc additive manufacturing (T-WAAM), *Mater. Des.* 213 (2022) 110270, <https://doi.org/10.1016/j.matdes.2021.110270>.
- [7] B. Wu, et al., Enhanced interface strength in steel-nickel bimetallic component fabricated using wire arc additive manufacturing with interweaving deposition strategy, *J. Mater. Sci. Technol.* 52 (2020) 226–234, <https://doi.org/10.1016/j.jmst.2020.04.019>.
- [8] S. Chandrasekaran, S. Hari, M. Amirthalingam, Wire arc additive manufacturing of functionally graded material for marine risers, *Mater. Sci. Eng., A* 792 (June) (2020) 139530, <https://doi.org/10.1016/j.msea.2020.139530>.
- [9] J.L. Galán Argumedo, M. Mahmoudiniya, T.E. Reinton, L.A.I. Kestens, M.J. Hermans, V.A. Popovich, Functional grading of low alloy steel to 316 L by wire arc additive manufacturing – microstructural and mechanical characterization of bi-metal interface, *J. Mater. Process. Technol.* 325 (Apr. 2024) 118305, <https://doi.org/10.1016/j.jmatprotec.2024.118305>.
- [10] J.L. Galán Argumedo, et al., Fatigue crack propagation in functionally graded bi-material steel obtained through wire-arc additive manufacturing, *Int. J. Fatig.* 194 (September 2024) (May 2025) 108819, <https://doi.org/10.1016/j.ijfatigue.2025.108819>.
- [11] A. Ermakova, *Structural Integrity Assessment of Wire Arc Additively Manufactured Low Carbon Steel Components for Marine Applications*, University of Strathclyde, Glasgow, 2023.
- [12] T. Ron, O. Dolev, A. Leon, A. Shirizly, E. Aghion, Effect of phase transformation on stress corrosion behavior of additively manufactured austenitic stainless steel produced by directed energy deposition, *Materials* 14 (1) (2021) 1–12, <https://doi.org/10.3390/ma14010055>.
- [13] X. Wenkai, et al., Effect of heat input on cryogenic toughness of 316LN austenitic stainless steel NG-MAG welding joints with large thickness, *Mater. Des.* 86 (2015) 160–167, <https://doi.org/10.1016/j.matdes.2015.07.115>.
- [14] N. Switzer, Z. Yu, Austenitic stainless steel cladding interface microstructures evaluated for petrochemical applications, *Weld. J.* 98 (2) (Feb. 2019) 50S–61S, <https://doi.org/10.29391/2019.98.004>.
- [15] D. Wang, X. Sun, Y. Jiang, X. Chang, X. Yonglei, Review on the application of stainless-clad bimetallic steel in the marine environment, *Anti-corrosion Methods & Mater.* 71 (2) (2024) 132–142, <https://doi.org/10.1108/ACMM-06-2023-2832>.
- [16] D. Frey, J. Palladino, J. Sullivan, M. Atherton, Part count and design of robust systems, *Syst. Eng.* 10 (3) (Sep. 2007) 203–221, <https://doi.org/10.1002/sys.20071>.
- [17] A. Taşdemir, S. Nohut, An overview of wire arc additive manufacturing (WAAM) in shipbuilding industry. *Ships and Offshore Structures*, Taylor and Francis Ltd, 2020, pp. 1–18, <https://doi.org/10.1080/17445302.2020.1786232>.
- [18] K. Lipiäinen, et al., Manufacturing and mechanical performance of a large-scale stainless steel vessel fabricated by wire-arc direct energy deposition, *Mater. Des.* 243 (May) (2024), <https://doi.org/10.1016/j.matdes.2024.113044>.
- [19] J.G. Rafferty, D. Gill, R. Kapur, Disrupting the metallics domain in pressure vessel and piping manufacture-advanced manufacturing in the oil and gas sector, in: *Volume 5: High-Pressure Technology; ASME Nondestructive Evaluation, Diagnosis and Prognosis Division (NDPD); SPC Track for Senate*, Jul. 2017, pp. 1–7, <https://doi.org/10.1115/PVP2017-65840>.
- [20] J.N. DuPont, C.S. Kusko, Technical note: martensite formation in austenitic/ferritic dissimilar alloy welds, *Weld. J.* 86 (2) (2007).
- [21] Z.H. Wang, B.Y. Xu, C.Q. Ye, Study of the martensite structure at the weld interface and the fracture-toughness of dissimilar metal joints, *Weld. J.* 72 (8) (1993) S397–S402.
- [22] M. Mukherjee, T.K. Pal, Influence of heat input on martensite formation and impact property of ferritic-austenitic dissimilar weld metals, *J. Mater. Sci. Technol.* 28 (4) (2012) 343–352, [https://doi.org/10.1016/S1005-0302\(12\)60066-8](https://doi.org/10.1016/S1005-0302(12)60066-8).
- [23] T.W. Nelson, J.C. Lippold, M.J. Mills, Investigation of boundaries and structures in dissimilar metal welds, *Sci. Technol. Weld. Join.* 3 (5) (1998) 249–255, <https://doi.org/10.1179/stw.1998.3.5.249>.
- [24] Q. Wang, et al., Study of type-II boundary behavior during SA508-3/EQ309L overlay weld interfacial failure process, *J. Mater. Process. Technol.* 247 (December 2016) 64–72, <https://doi.org/10.1016/j.jmatprotec.2017.04.009>, 2017.
- [25] T.W. Nelson, J.C. Lippold, M.J. Mills, Nature and evolution of the fusion boundary in ferritic-austenitic dissimilar metal welds - Part 2: on-cooling transformations, *Weld. J.* 79 (10) (2000).
- [26] M.R.U. Ahsan, et al., Heat-treatment effects on a bimetallic additively-manufactured structure (BAMS) of the low-carbon steel and austenitic-stainless steel, *Addit. Manuf.* 32 (2020) 1–25, <https://doi.org/10.1016/j.addma.2020.101036>.
- [27] G. Ben Salem, S. Chapuliot, A. Blouin, P. Bompard, C. Jacquemoud, Brittle fracture analysis of Dissimilar Metal Welds between low-alloy steel and stainless steel at low temperatures, *Procedia Struct. Integr.* 13 (2018) 619–624, <https://doi.org/10.1016/j.prostr.2018.12.102>.
- [28] P. Dirisu, S. Ganguly, A. Mehmanparast, F. Martina, S. Williams, Analysis of fracture toughness properties of wire + arc additive manufactured high strength low alloy structural steel components, *Mater. Sci. Eng., A* 765 (June) (2019) 138285, <https://doi.org/10.1016/j.msea.2019.138285>.
- [29] D. Kumar, S. Jhavar, A. Arya, K.G. Prashanth, S. Suwas, Mechanisms controlling fracture toughness of additively manufactured stainless steel 316L, *Int. J. Fract.* 235 (1) (2022) 61–78, <https://doi.org/10.1007/s10077-021-00574-3>.
- [30] T. Sang Byung, T. Lach, D. Collins, *Effect of Thermal Aging in Stainless Steel Welds: 2nd Year Progress Report of I-NERI Collaboration*, 2017.
- [31] W.J. Mills, Fracture toughness of type 304 and 316 stainless steels and their welds, *Int. Mater. Rev.* 42 (2) (1997) 45–82, <https://doi.org/10.1179/imr.1997.42.2.45>.
- [32] J. Talonen, H. Hänninen, Formation of shear bands and strain-induced martensite during plastic deformation of metastable austenitic stainless steels, *Acta Mater.* 55 (18) (2007) 6108–6118, <https://doi.org/10.1016/j.actamat.2007.07.015>.
- [33] ISO, *NEN-ISO 12135:2021 Metallic Materials - Unified Method of Test for the Determination of Quasistatic Fracture Toughness*, 2022. Switzerland.
- [34] ASTM, *E1820 - 20b Standard Test Method for Measurement of Fracture Toughness*, ASTM International, West Conshohocken, 2020 [Online]. Available: www.astm.org.
- [35] J.R. Rice, A path independent integral and the approximate analysis of strain concentration by notches and cracks, *J. Appl. Mech. Trans. ASME* 35 (2) (1968) 379–388, <https://doi.org/10.1115/1.3601206>.
- [36] Z.H. Jin, N. Noda, Crack-tip singular fields in nonhomogeneous materials, *J. Appl. Mech. Trans. ASME* 61 (3) (1994) 738–740, <https://doi.org/10.1115/1.2901529>.
- [37] F. Erdogan, B.H. Wu, The surface crack problem for a plate with functionally graded properties, *J. Appl. Mech. Trans. ASME* 64 (3) (1997) 449–456, <https://doi.org/10.1115/1.2788914>.
- [38] J. Chen, L. Wu, S. Du, A modified J integral for functionally graded materials, *Mech. Res. Commun.* 27 (3) (May 2000) 301–306, [https://doi.org/10.1016/S0093-6413\(00\)00096-3](https://doi.org/10.1016/S0093-6413(00)00096-3).
- [39] T. Honein, G. Herrmann, Conservation laws in nonhomogeneous plane elastostatics, *J. Mech. Phys. Solid.* 45 (5) (May 1997) 789–805, [https://doi.org/10.1016/S0022-5096\(96\)00087-7](https://doi.org/10.1016/S0022-5096(96)00087-7).
- [40] D. Weichert, M. Schulz, J-integral concept for multi-phase materials, *Comput. Mater. Sci.* 1 (3) (1993) 241–248, [https://doi.org/10.1016/0927-0256\(93\)90016-G](https://doi.org/10.1016/0927-0256(93)90016-G).
- [41] S. Ghorbanpour, et al., Effect of microstructure induced anisotropy on fatigue behaviour of functionally graded Inconel 718 fabricated by additive manufacturing, *Mater. Char.* 179 (Sep) (2021), <https://doi.org/10.1016/j.matchar.2021.111350>.
- [42] AWS, *AWS a5.18/a5.18m:2005 specification for carbon steel electrodes and rods for gas shielded arc welding*, Miami, USA: ANSI (2005).
- [43] AWS, *AWS a5.9/a5.9m:2012 specification for bare stainless steel welding electrodes and rods*, Miami, USA: AWS A5.9/A5.9M:2012, American Welding Society, 2012.
- [44] 3Dprint AM 46, *Böhler Welding by Voestalpine*, 2018, 2018 [Online]. Available: <https://www.vabw-service.com/voestalpine/>.
- [45] 3Dprint AM 316L, *Böhler Welding by Voestalpine*, 2019, 2019 [Online]. Available: <https://www.vabw-service.com/voestalpine/>.
- [46] *NEN-ISO, EN-ISO 6892-1:2019 Metallic Materials - Tensile Testing - Part 1: Method of Test at Room Temperature*, december 2019. Belgium, 2019.
- [47] S. Ghorbanpour, et al., Effect of microstructure induced anisotropy on fatigue behaviour of functionally graded Inconel 718 fabricated by additive manufacturing, *Mater. Char.* 179 (July) (2021) 111350, <https://doi.org/10.1016/j.matchar.2021.111350>.
- [48] W.J. Mills, Heat-to-heat variations in the fracture toughness of austenitic stainless steels, *Eng. Fract. Mech.* 30 (4) (1988) 469–492, [https://doi.org/10.1016/0013-7944\(88\)90058-6](https://doi.org/10.1016/0013-7944(88)90058-6).
- [49] A. Ermakova, A. Mehmanparast, S. Ganguly, J. Razavi, F. Berto, Investigation of mechanical and fracture properties of wire and arc additively manufactured low carbon steel components, *Theor. Appl. Fract. Mech.* 109 (May) (2020) 102685, <https://doi.org/10.1016/j.tafmec.2020.102685>.
- [50] W.L. Costin, O. Lavigne, A. Kotousov, A study on the relationship between microstructure and mechanical properties of acicular ferrite and upper bainite,

- Mater. Sci. Eng., A 663 (2016) 193–203, <https://doi.org/10.1016/j.msea.2016.03.103>.
- [51] M.S. Pham, B. Dovggy, P.A. Hooper, Twinning induced plasticity in austenitic stainless steel 316L made by additive manufacturing, Mater. Sci. Eng., A 704 (April) (2017) 102–111, <https://doi.org/10.1016/j.msea.2017.07.082>.
- [52] F.K. Yan, G.Z. Liu, N.R. Tao, K. Lu, Strength and ductility of 316L austenitic stainless steel strengthened by nano-scale twin bundles, Acta Mater. 60 (3) (Feb. 2012) 1059–1071, <https://doi.org/10.1016/j.actamat.2011.11.009>.
- [53] J. Talonen, Effect of Strain-Induced α' -martensite Transformation on Mechanical Properties of Metastable Austenitic Stainless Steels, PhD, 2007.
- [54] A. Das, Revisiting stacking fault energy of steels, Metall. Mater. Trans. A Phys. Metall. Mater. Sci. 47 (2) (2016) 748–768, <https://doi.org/10.1007/s11661-015-3266-9>.
- [55] G. Meric de Bellefon, J.C. van Duysen, K. Sridharan, Composition-dependence of stacking fault energy in austenitic stainless steels through linear regression with random intercepts, J. Nucl. Mater. 492 (2017) 227–230, <https://doi.org/10.1016/j.jnucmat.2017.05.037>.
- [56] J.A. Self, D.L. Olson, G.R. Edwards, The Stability of Austenitic Weld Metal, NBS publication on Cryogenic Properties of Metals, 1987, pp. 181–189.
- [57] A. Saeed-Abkari, L. Mosecker, A. Schwedt, W. Bleck, Characterization and prediction of flow behavior in high-manganese twinning induced plasticity steels: Part I. mechanism maps and work-hardening behavior, Metall. Mater. Trans. A Phys. Metall. Mater. Sci. 43 (5) (2012) 1688–1704, <https://doi.org/10.1007/s11661-011-0993-4>.
- [58] M. Madivala, A. Schwedt, S.L. Wong, F. Roters, U. Prahl, W. Bleck, Temperature dependent strain hardening and fracture behavior of TWIP steel, Int. J. Plast. 104 (February) (2018) 80–103, <https://doi.org/10.1016/j.ijplas.2018.02.001>.
- [59] P. Thome, M. Schneider, V.A. Yardley, E.J. Payton, G. Eggeler, Crystallographic analysis of plate and lath martensite in Fe-Ni alloys, Crystals 12 (2) (2022) 11–13, <https://doi.org/10.3390/cryst12020156>.
- [60] T. Maki, Morphology and Substructure of Martensite in Steels, Woodhead Publishing Limited, 2012.
- [61] K. Verbeke, L. Barbé, D. Raabe, Evaluation of the crystallographic orientation relationships between FCC and BCC phases in TRIP steels, ISIJ Int. 49 (10) (2009) 1601–1609, <https://doi.org/10.2355/isijinternational.49.1601>.
- [62] V. Tari, A.D. Rollett, H. Beladi, Back calculation of parent austenite orientation using a clustering approach, J. Appl. Crystallogr. 46 (1) (2013) 210–215, <https://doi.org/10.1107/S002188981204914X>.
- [63] S. Morito, X. Huang, T. Furuhashi, T. Maki, N. Hansen, The morphology and crystallography of lath martensite in alloy steels, Acta Mater. 54 (19) (Nov. 2006) 5323–5331, <https://doi.org/10.1016/j.actamat.2006.07.009>.
- [64] P.P. Suikkanen, C. Cayron, A.J. DeArdo, L.P. Karjalainen, Crystallographic analysis of martensite in 0.2C-2.0Mn-1.5Si-0.6Cr steel using EBSD, J. Mater. Sci. Technol. 27 (10) (Oct. 2011) 920–930, [https://doi.org/10.1016/S1005-0302\(11\)60165-5](https://doi.org/10.1016/S1005-0302(11)60165-5).
- [65] S. Allain, J.P. Chateau, O. Bouaziz, S. Migot, N. Guelton, Correlations between the calculated stacking fault energy and the plasticity mechanisms in Fe-Mn-C alloys, Mater. Sci. Eng., A 387–389 (1) (2004) 158–162, <https://doi.org/10.1016/j.msea.2004.01.059>, 2 SPEC. ISS.
- [66] S. Curtze, V.T. Kuokkala, Dependence of tensile deformation behavior of TWIP steels on stacking fault energy, temperature and strain rate, Acta Mater. 58 (15) (2010) 5129–5141, <https://doi.org/10.1016/j.actamat.2010.05.049>.
- [67] I. Gutierrez-Urrutia, D. Raabe, Dislocation and twin substructure evolution during strain hardening of an Fe-22 wt.% Mn-0.6 wt.% C TWIP steel observed by electron channeling contrast imaging, Acta Mater. 59 (16) (2011) 6449–6462, <https://doi.org/10.1016/j.actamat.2011.07.009>.
- [68] H. Beladi, I.B. Timokhina, Y. Estrin, J. Kim, B.C. De Cooman, S.K. Kim, Orientation dependence of twinning and strain hardening behaviour of a high manganese twinning induced plasticity steel with polycrystalline structure, Acta Mater. 59 (20) (2011) 7787–7799, <https://doi.org/10.1016/j.actamat.2011.08.031>.
- [69] D. Barbier, et al., EBSD for analysing the twinning microstructure in fine-grained TWIP steels and its influence on work hardening, J. Microsc. (2009) no. hal-02402444.
- [70] P.J. Jacques, Q. Furnémont, F. Lani, T. Pardoen, F. Delannay, Multiscale mechanics of TRIP-assisted multiphase steels: I. Characterization and mechanical testing, Acta Mater. 55 (11) (2007) 3681–3693, <https://doi.org/10.1016/j.actamat.2007.02.029>.
- [71] P. Jacques, Q. Furnémont, A. Mertens, F. Delannay, On the sources of work hardening in multiphase steels assisted by transformation-induced plasticity, Philos. Mag. A Phys. Condens. Matter, Struct. Defects Mech. Prop. 81 (7) (2001) 1789–1812, <https://doi.org/10.1080/01418610108216637>.
- [72] G. Krauss, Martensite in steel: strength and structure, Mater. Sci. Eng., A 273 (275) (1999) 40–57, [https://doi.org/10.1016/S0921-5093\(99\)00288-9](https://doi.org/10.1016/S0921-5093(99)00288-9).
- [73] M. Shamsujjoha, Evolution of microstructures, dislocation density and arrangement during deformation of low carbon lath martensitic steels, Mater. Sci. Eng., A 776 (Mar. 2020) 139039, <https://doi.org/10.1016/j.msea.2020.139039>.
- [74] C. Du, R. Petrov, M.G.D. Geers, J.P.M. Hoefnagels, Lath martensite plasticity enabled by apparent sliding of substructure boundaries, Mater. Des. 172 (2019) 1–12, <https://doi.org/10.1016/j.matdes.2019.107646>.
- [75] J. Chen, Y. Verreman, J. Lanteigne, On fracture toughness JIC testing of martensitic stainless steels, 13th Int. Conf. Fract. 2013, ICF 5 (2013) 3561–3569, 2013.
- [76] S. Kumar, P.K. Singh, K.N. Karn, V. Bhasin, Experimental investigation of local tensile and fracture resistance behaviour of dissimilar metal weld joint: SA508 Gr.3 Cl.1 and SA312 Type 304LN, Fatig. Fract. Eng. Mater. Struct. 40 (2) (2017) 190–206, <https://doi.org/10.1111/ffe.12484>.
- [77] H. Ming, J. Wang, E.-H. Han, Comparative study of microstructure and properties of low-alloy-steel/nickel-based-alloy interfaces in dissimilar metal weld joints prepared by different GTAW methods, Mater. Char. 139 (May 2018) 186–196, <https://doi.org/10.1016/j.matchar.2018.02.044>.
- [78] H. Ming, et al., Microstructure, local mechanical properties and stress corrosion cracking susceptibility of an SA508-52M-316LN safe-end dissimilar metal weld joint by GTAW, Mater. Sci. Eng., A 669 (Jul. 2016) 279–290, <https://doi.org/10.1016/j.msea.2016.05.101>.
- [79] J. Hollomon, Tensile deformation, Trans. Metall. Soc. AIME 162 (1945) 268–290.